12-2017

A Parameterized Simulation of Doppler Lidar

David B. Chester
Utah State University

A PARAMETERIZED SIMULATION OF DOPPLER LIDAR

by

David B. Chester

A thesis submitted in partial fulfillment
of the requirements for the degree

of

MASTER OF SCIENCE

in

Electrical Engineering

Approved:

Scott E. Budge, Ph.D. Major Professor	Jacob Gunther, Ph.D. Committee Member
Charles M. Swenson, Ph.D. Committee Member	Mark R. McLellan, Ph.D. Vice President for Research and Dean of the School of Graduate Studies

UTAH STATE UNIVERSITY
Logan, Utah

2017

ABSTRACT

A Parameterized Simulation of Doppler Lidar

by

David B. Chester, Master of Science

Utah State University, 2017

Major Professor: Scott E. Budge, Ph.D.
Department: Electrical and Computer Engineering

Upcoming missions to explore planetary bodies in the solar system will require accurate position and velocity data during descent in order to land safely at a predesignated site. A Doppler lidar instrument could provide measurements of the altitude, attitude, and velocity of the landing vehicle to supplement the data collected by other instruments. A flexible simulation tool would aid the tasks of designing and testing the functionality of such an instrument.

LadarSIM is a robust parameterized simulation tool developed for time of flight lidar at Utah State University's Center for Advanced Imaging Ladar. This thesis outlines how LadarSIM was modified to include a simulation of Doppler lidar. A study is performed using LadarSIM to determine the effects of varying the transmission power, aperture diameter, and fast Fourier transform (FFT) size of a Doppler lidar. Point clouds of landing scenarios generated by the simulation with different scanning patterns are shown.

(70 pages)

PUBLIC ABSTRACT

A Parameterized Simulation of Doppler Lidar

David B. Chester

Upcoming missions to explore planetary bodies in the solar system will require accurate position and velocity data during descent in order to land safely at a predesignated site. A Doppler lidar instrument could provide measurements of the altitude, attitude, and velocity of the landing vehicle to supplement the data collected by other instruments. A flexible simulation tool would aid the tasks of designing and testing the functionality of such an instrument.

LadarSIM is a robust parameterized simulation tool developed for time of flight lidar at Utah State University's Center for Advanced Imaging Ladar. This thesis outlines how LadarSIM was modified to include a simulation of Doppler lidar. A study is performed using LadarSIM to determine the effects of varying certain parameters of a Doppler lidar system. Point clouds of landing scenarios generated by the simulation with different scanning patterns are shown.

ACKNOWLEDGMENTS

I would like to thank my wife, Lucy Chester, whose love and support have made it possible for me to finish my degree. It should be noted that she is responsible for nearly every correct use of a comma in this thesis. I would like to thank my parents, Greg and Susan Chester, for imparting to me the importance of a higher education and enabling me through their support and generosity to pursue my educational goals and develop my talents throughout my life.

I would also like to thank some of the teachers who have impacted me. I'd like to thank my 6^{th} grade teacher Kwin Walker who helped me to see potential in myself. Each member of my committee has had a great impact on my development as an engineer. I'm grateful to Dr. Charles Swenson who helped me get my first job in the engineering field as a student engineering assistant at the Space Dynamics Lab. I'd like to thank Dr. Jacob Gunther for helping with my independent study. I'm grateful to Dr. Scott Budge for guiding my research and encouraging me to publish my work.

David B. Chester

CONTENTS

LIST OF TABLES

LIST OF FIGURES

CHAPTER 1

INTRODUCTION

1.1 Overview

Recent and upcoming missions for the exploration of solar system bodies require accurate position and velocity data during the descent phase to ensure safe landing at predesignated sites. Because of inertial measurement unit (IMU) drift during travel, the data provided by the IMU may not be reliable. One solution proposed by NASA is the use of a frequency modulated continuous wave (FMCW) Doppler lidar system during the landing phase to provide additional information about attitude, position, and velocity to contribute to a successful landing [2–4]. The optimization and comparison of potential configurations of such a system would be greatly aided by an appropriate simulation tool.

LadarSIM is a robust parametrized simulation tool for time of flight lidar developed at Utah State University's Center for Advanced Imaging Ladar over the past decade and a half [5, 6]. LadarSIM has the flexibility to simulate a wide range of time of flight lidar systems with varying beam and scanner patterns as well as parametrized transmitters and receivers. These simulated systems can be evaluated using scenarios consisting of user specified terrain, targets, and flight paths.

The research for this thesis had three objectives. First, to add a parameterized simulation of an FMCW lidar transmitter and receiver, second, to utilize that simulation to perform a trade-off study to determine the effects of varying laser transmission power, beam divergence, aperture diameter, and Fast Fourier Transform (FFT) size on a Doppler lidar system, and third, to use the simulation to compare traditional and novel scanning patterns in planetary landing scenarios.

In order to meet the research objectives of this thesis, LadarSIM was modified to include a simulation of an FMCW Doppler lidar transceiver and detection process which

can be configured to model the behavior of a range of instruments. This included creating several new graphical user interfaces (GUIs) to allow a user to specify the desired transceiver parameters. LadarSIM's geometry simulation was modified to calculate and store the radial velocity measurements needed to simulate a Doppler lidar. A model of a Doppler lidar transceiver was created including the calculation of the power, frequency, and phase of the laser radiation returning from a target and a detection process was coded to detect the generated signal. This simulation was used to investigate the effects of varying the laser transmission power, aperture diameter, and FFT size of a lidar. Finally the simulation was used to compare scanning patterns to potentially be used by a planetary landing vehicle during the descent phase of its mission.

The simulation developed for this thesis is a useful tool for the development of Doppler lidar systems with a wide range of transceiver characteristics and, by leveraging the existing scanner simulation ability of LadarSIM, nearly arbitrary beam and scanning parameters. The information gained from the trade-off study will provide valuable insight for someone designing or selecting a Doppler lidar system to meet mission requirements. The point clouds generated in the exploration of novel scanning patterns give an idea of the potential utility of a Doppler lidar system for terrain mapping, navigation, and hazard avoidance.

1.2 Chapter Outlines

This thesis will describe the theory of FMCW lidar, how LadarSIM was expanded to add a simulation of Doppler lidar, and present results from LadarSIM's Doppler lidar simulation. To achieve this, the thesis will be structured as follows: Chapter 2 will describe the theory behind FMCW radar detection and show how the same basic concepts can be applied to a lidar system. Chapter 3 will present some background information on LadarSIM and then show how it was modified to include a simulation of Doppler lidar. Chapter 4 will present a trade-off study exploring the effects of laser transmission power, beam divergence, aperture diameter, and FFT size on a Doppler lidar system. Chapter 5 will discuss novel scanning patterns and present point clouds generated by LadarSIM for those patterns. Chapter 6 is the conclusion of the thesis and will also discuss the potential for future work.

CHAPTER 2
FREQUENCY MODULATED CONTINUOUS WAVE DETECTION

2.1 FMCW Lidar

Booker [7] presents the theory behind Frequency Modulated Continuous Wave (FMCW) radar detection. The same theory applies to FMCW lidar by making the appropriate changes in the system hardware. For example, the antennae would be replaced with a telescope etc. This section will follow the development of Booker making appropriate changes to apply the detection process to FMCW lidar.

2.1.1 Basic Principles

FMCW detection refers to a lidar system in which a laser beam is constantly emitted while being periodically modulated in amplitude with detection based on the difference between the modulation frequency of the transmitted and echoed light. The wavelength of the transmitted laser is constant but the frequency at which the laser amplitude is modulated, is varied. A continuous wave lidar in which a single laser source serves as both the transmitter and local oscillator (LO) is, generally speaking, a homodyne lidar. FMCW lidar systems often leverage a homodyne architecture.

An FMCW lidar uses a continuous wave signal which is modulated in amplitude over a range of frequencies creating a linear chirp. This chirped signal is radiated to the target and an echo returns after time T_p, which is the time it takes for the signal to reach the target and reflected energy to return to the lidar. Figure 2.1 illustrates a chirped signal, shown with a solid line, and the return signal delayed by T_p, shown with a dashed line. In this figure f_b refers to the difference in frequency of the two signals at a given time.

It is clear that the distance to the target can be calculated with T_p. In an FMCW system, T_p is determined by measuring the beat frequency f_b. To do this, a portion of the

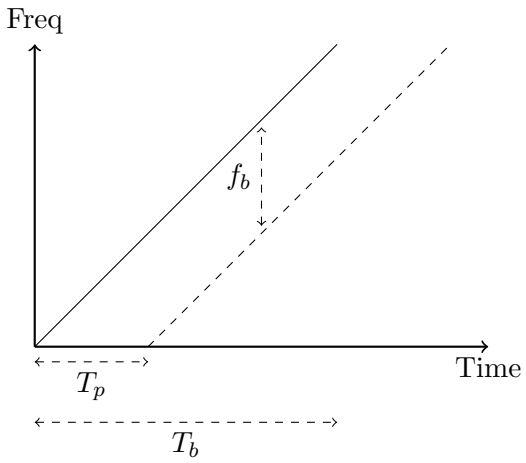

Fig. 2.1: Transmit and Receive Doppler Shift

signal produced by the LO is mixed with the returned echo producing f_b. A signal chirped in frequency can be expressed as

$$v_{fm}(t) = A_c cos[\omega_c t + \frac{A_b}{2} t^2], \tag{2.1}$$

where A_c is the amplitude of the laser, A_b is a constant of proportionality between the change in frequency over the chirp or chirp slope, ω_b, and the chirp time such that $\omega_b = A_b t$. The mixture of the transmitted and received signals can be expressed as

$$v_{fm}(t - T_p)v_{fm}(t) = A_c^2 cos[\omega_c t + \frac{A_b}{2} t^2] cos[\omega_c (t - T_p) + \frac{A_b}{2}(t - T_p)^2]. \tag{2.2}$$

This simplifies to

$$v_{out}(t) = A_c^2 (cos[(2\omega_c - A_b T_p)t + A_b t^2 + (\frac{A_b}{2} T_p^2 - \omega_c T_p)] + cos[A_b T_p t + (\omega_c T_p - \frac{A_b}{2} T_p^2)]). \tag{2.3}$$

It is desirable to isolate the second term in (2.3) because it is the the beat signal. The first cosine term is an FM chirp at about twice the carrier frequency and is in most cases conveniently filtered out because it is above the cutoff frequency of the receiver components.

To obtain the f_b from the beat signal the phase term is differentiated with time,

$$f_b = \frac{1}{2\pi}\frac{d}{dt}[A_b T_b t + (\omega_c T_p - \frac{A_b}{2}T_p^2)], \tag{2.4}$$

resulting in

$$f_b = (\frac{A_b}{2\pi})T_p. \tag{2.5}$$

2.1.2 FMCW Detection

As discussed above, the most common way to obtain the beat frequency f_b is to take the product of the transmitted chirp signal and the received signal and filter to isolate the constant frequency beat. The FFT is a common method of spectral analysis employed in FMCW lidar to measure f_b.

Given a chirp duration, T_b(s), and assuming that $T_b \gg T_p$, the maximum resolution of the beat frequency is $2/T_b$(Hz). Figure 2.1 shows a chirp which meets that criterion. The resolution bandwidth of a signal, δf_b, is commonly defined between its 3 dB points. For the truncated chirp case δf_b coincides with a region of width $1/T_b$ centered on f_b. Figure 2.2(a) shows a sinusoidal signal with duration T_b. The spectrum of that signal is shown in Fig. 2.2(b) and has a resolution bandwidth of $1/T_b$.

The chirp bandwidth is the total change in frequency for the chirp, Δf. Clearly the slope of the chirp is the chirp bandwidth divided by the chirp time, $\Delta f/T_b$. Equation 2.5 can then be restated

$$f_b = A_b T_p = \frac{\Delta f}{T_b} T_p. \tag{2.6}$$

Intuitively, T_p is the round trip time from the antennae to the target and back

$$T_p = \frac{2R}{c}, \tag{2.7}$$

where c is the speed of light. The classical FMCW formula is obtained by substituting into (2.6):

$$f_b = \frac{\Delta f}{T_b}\frac{2R}{c}, \tag{2.8}$$

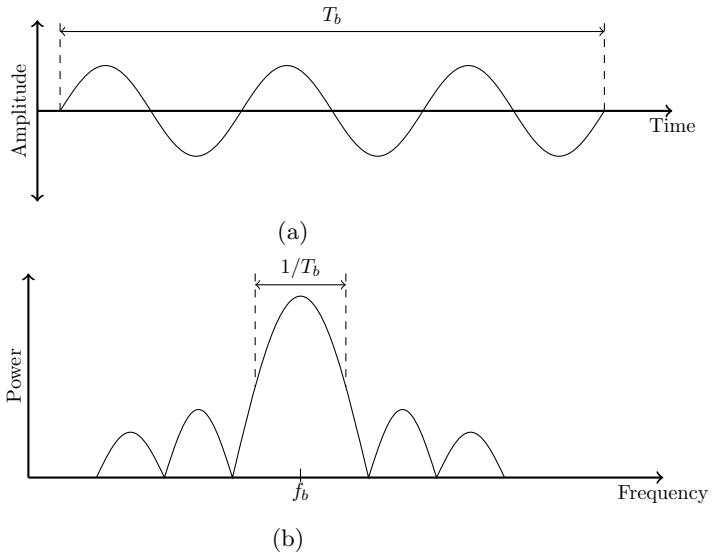

Fig. 2.2: Illustration of how chirp duration limits the resolution in the frequency domain. (a) Truncated sinusoidal signal. (b) Frequency domain representation of the truncated sinusoid.

relating the beat frequency to the range. Solving for range yields

$$R = \frac{T_b c}{2\Delta f} f_b. \tag{2.9}$$

Equation 2.9 relates range to beat frequency. The same equation can be used to related range resolution δf and chirp bandwidth:

$$\delta R = \frac{T_b c}{2\Delta f} \delta f = \frac{c}{2\Delta f}, \tag{2.10}$$

where the frequency resolution δf is approximately equal to $1/T_b$.

2.1.3 Doppler Effect in FMCW

So far the development in this section has assumed a stationary lidar and target. The case where the lidar, the target, or both are moving will now be examined. The Doppler effect describes the change in observed and transmitted frequencies when the distance be-

tween the two is changing. The relationship between the transmitted frequency, f_c, and the received frequency, f_r can be expressed

$$f_r = \frac{c + v_t}{c + v_s} f_c, \tag{2.11}$$

where v_t is the velocity of the target and v_s is the velocity of the source. From (2.11) it is simple to obtain an equation for the change in frequency, $f_r - f_c$, in relation to the difference in velocity of the source and target, Δv:

$$f_r - f_c = \frac{\Delta v}{c} f_s = \frac{\Delta v}{\lambda}, \tag{2.12}$$

where λ is the laser wavelength.

For the following development, the radial velocity v_r(m/s) will represent the velocity term causing the Doppler effect. Modifying (2.1) to incorporate the Doppler shift of the echo signal yields:

$$v_{fm}(t - T_p) = A_c cos[\omega_c(t - T_p) + \frac{A_b}{2}(t - T_p)^2 - \frac{2v_r}{c}\omega_c(t - T_p)]. \tag{2.13}$$

The new beat frequency then is the same as derived in (2.5) and (2.6) shifted by the Doppler frequency, f_d:

$$f_b = \frac{2v_r}{c} f_c - \frac{A_b}{2\pi} T_p = f_d - \frac{A_b}{2\pi} T_p. \tag{2.14}$$

For a chirp with positive A_b, an up-chirp, the beat frequency will be the difference between the Doppler frequency f_d and the beat frequency caused by the echo time or range frequency f_r. For a down-chirp, a negative slope, the beat frequency will be the sum of the Doppler frequency and the range frequency. In many radar applications it can be assumed that the Doppler frequency is lower than the range frequency leading to (2.15) and (2.16). If $f_d > f_b$, as is frequently the case in Lidar, the roles of f_d and f_b are reversed.

$$f_{b(Up)} = f_b - f_d \tag{2.15}$$

$$f_{b(Down)} = f_b + f_d \tag{2.16}$$

By using a triangle waveform the sum and difference frequencies can be obtained to isolated range and velocity measurements. Figure 2.3 illustrates the Doppler effect on an FMCW waveform transmitting a triangle wave pattern. Figures 2.3(a) and 2.3(b) show the transmitted frequencies with a solid line and the received frequencies with a dashed line. Note the dashed lines are both shifted in time proportionally with the distance between the lidar and the target but the dashed line in Fig. 2.3(b) is also shifted by the Doppler frequency. Figures 2.3(c) and 2.3(d) present the corresponding beat frequencies. By observing Fig. 2.3(d) it is straightforward to obtain expressions for f_r and f_d by averaging and differencing (2.15) and (2.16):

$$f_r = \frac{f_{b(Up)} - f_{b(Down)}}{2}, \tag{2.17}$$

$$f_d = \frac{f_{b(Up)} + f_{b(Down)}}{2}. \tag{2.18}$$

The sign of f_d is determined by the direction of motion. If the range is getting smaller f_d will be positive and if the range is getting larger f_d will be negative.

2.2 FMCW Lidar Processing

The two main differences between FMCW lidar and radar are the modulation frequencies and the wavelength of the radiation. One consequence of this is that the Doppler frequency is usually higher than the beat frequency, leading to some minor modifications to the equations in Section 2.1. Most importantly, the relationship between beat frequency of the up-chirp with the Doppler frequency is better expressed as:

$$f_{b(Up)} = f_d - f_b. \tag{2.19}$$

By adding a period of constant frequency between up and down chirps in the chirp

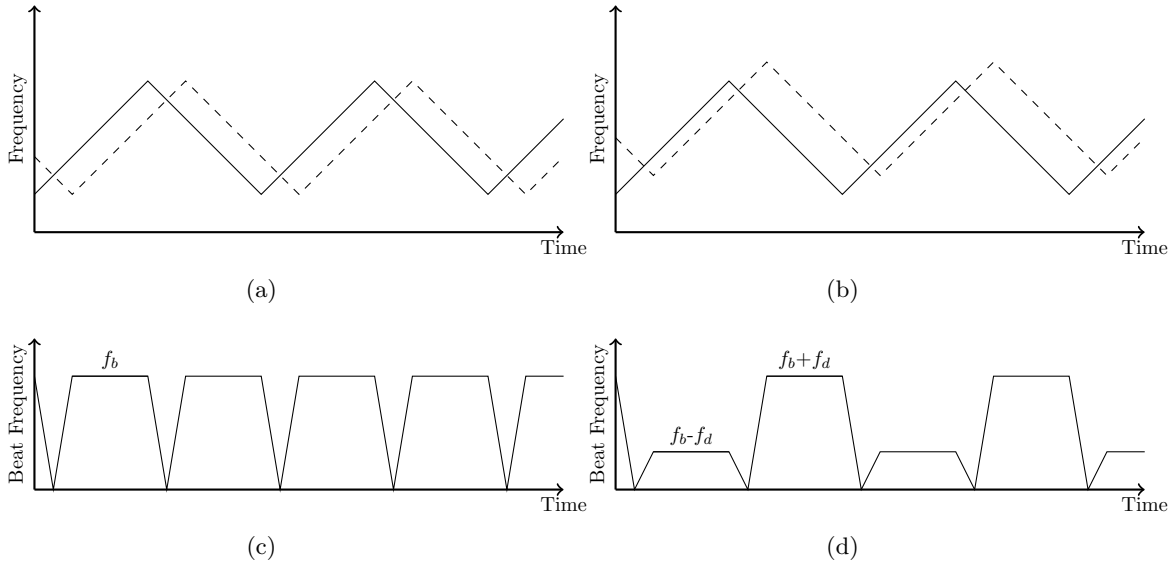

Fig. 2.3: Doppler effect on FMCW lidar. (a) Transmitted and received chirp signals without Doppler effect. (b) Transmitted and received chirp signals with Doppler effect. (c) Beat frequencies without the Doppler Effect. (d) Beat frequencies with the Doppler effect.

process illustrated in Fig. 2.3 a direct measurement of the Doppler frequency can be taken [8]. This modified chirp process is shown in Fig. 2.4. This process allows the system to measure frequencies: $f_{b(Up)}$ the up-chirp frequency, f_d the Doppler frequency, and $f_{b(Down)}$ the down-chirp frequency. The range information is encoded in the beat frequency f_r which is obtained from $f_{b(Up)}$ and $f_{b(Down)}$ by (2.17), substituting this result into (2.9) yields:

$$R = \frac{T_b c}{2\Delta f} \frac{f_{b(Up)} - f_{b(Down)}}{2}, \tag{2.20}$$

where Δf is the chirp bandwidth. Similarly, the velocity measurement can be obtained using the three available frequencies. One option is to use the measured Doppler frequency directly by substituting into (2.12) and solving for the velocity. The problem here is that the sign of f_d determines the direction of motion and the sign of f_d is not preserved in the FFT process. A better option is to use (2.18) to get f_d and substitute the result into (2.12) and solve for velocity resulting in:

$$V = \frac{\lambda}{2} \frac{f_{b(Up)} + f_{b(Down)}}{2}. \tag{2.21}$$

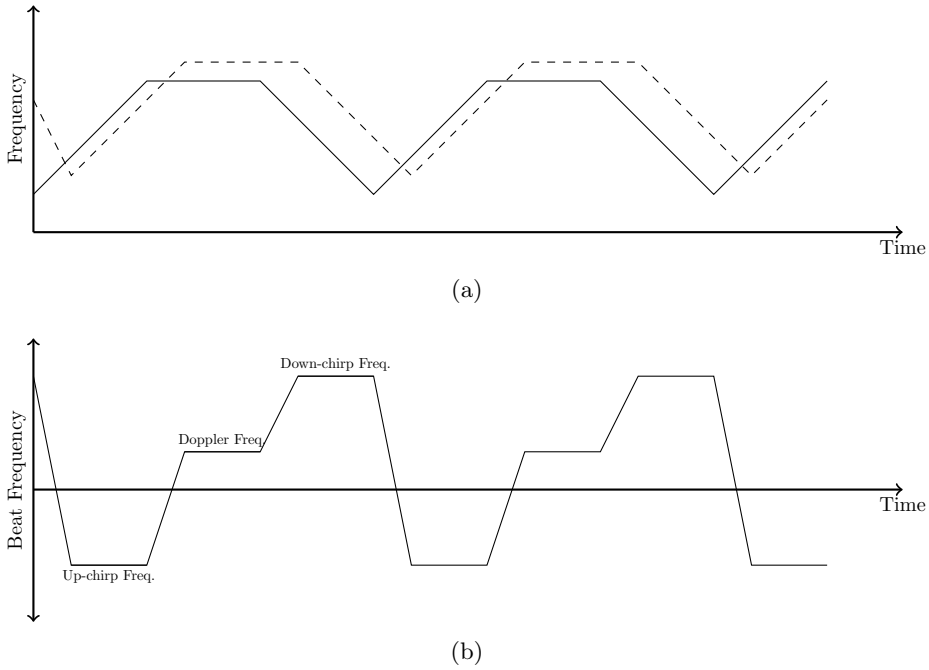

Fig. 2.4: Doppler Effect on FMCW lidar with up-chirp, Doppler, and down-chirp segments. (a) Transmitted and received frequencies. (b) Beat frequencies.

2.3 FMCW Lidar Architecture

In this section a number of detection architectures for FMCW lidar will be examined. Adany et al. provide an analysis of direct detection, heterodyne detection, as well as their proposed simplified homodyne detection, which will serve as the primary source of information in this section [1, 9].

2.3.1 Direct Detection Architecture

In an FMCW direct detection scheme, shown in Fig. 2.5, the signal from the modulation waveform generator is split. Part of the signal is used to modulate the amplitude of the laser, which is then amplified and sent to the telescope. The returning light is captured through the same telescope and converted into an electrical signal via a photodetector. The other part of the modulation signal is then mixed with the electrical signal from the detected returning light to perform de-chirping. An FFT is then taken on the de-chirped signal to find the beat frequency and the range information. The returning signal is weak so the

signal to noise ratio (SNR) at the output of the photodiode is primarily limited by thermal noise. Considering only thermal noise leads to the following expression for the maximum SNR:

$$SNR_{dir} \approx \frac{2\Re^2 P_{sig}^2}{\frac{4kTB_e}{R_L}}, \tag{2.22}$$

where $\Re$ is the photodiode responsivity, P_{sig} is the optical power of the received signal, k is Planck's constant, T is the absolute temperature, B_e is the electrical bandwidth, and R_L is the load resistance [9]. Analysis of (2.22) shows that for every dB reduction in the return signal power the SNR is reduced by 2 dB. This disadvantage leads to very quick degradation of the performance of a lidar system using direct detection as range increases.

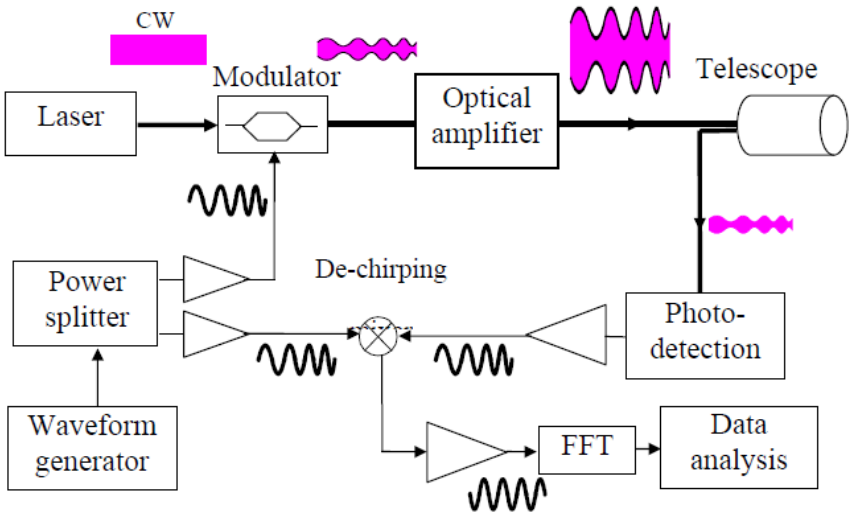

Fig. 2.5: Direct detection architecture [1].

2.3.2 Coherent Heterodyne Detection Architecture

In coherent heterodyne detection, shown in Fig. 2.6, the laser is split into two signals. One of these signals is modulated by the chirp waveform sent through an optical amplifier and out of the telescope. The other part of the the laser beam is used as the optical local oscillator. This LO signal is then shifted by an acousto-optic modulator to serve as the

intermediate frequency (IF) for coherent heterodyne detection. The IF is optically mixed with the returning signal from the telescope and the output of the optical mixer is fed into a balanced photodiode. The photodiode rejects the direct detection component. The output of the photodiode is filtered to isolate the heterodyne IF signal which is detected by an envelope detector. The IF signal is then mixed with the modulation waveform for de-chirping. An FFT is then performed on the de-chirped signal to recover the beat frequency.

Optically mixing the returned signal with the LO helps mitigate the thermal noise in the photodiode. But because the strong optical LO, the SNR is limited by the shot noise. The theoretical best SNR for a coherent heterodyne lidar is

$$SNR_{het} \approx \frac{\Re P_{sig}}{2qB_e}. \tag{2.23}$$

In this equation q is the electron charge. In coherent heterodyne detection the SNR is linearly proportional to the optical power, making it more suitable for low power operation. The most significant disadvantage of coherent heterodyne detection is its complexity. The IF must be set much higher than the baseband, often in the GHz. This necessitates high speed optical detection and radio frequency (RF) processing circuitry. The IF envelope detection process mixes the signal with RF noise which can further limit the SNR. Because of this, the theoretical SNR defined in (2.23) has not been obtained in a coherent heterodyne implementation [10].

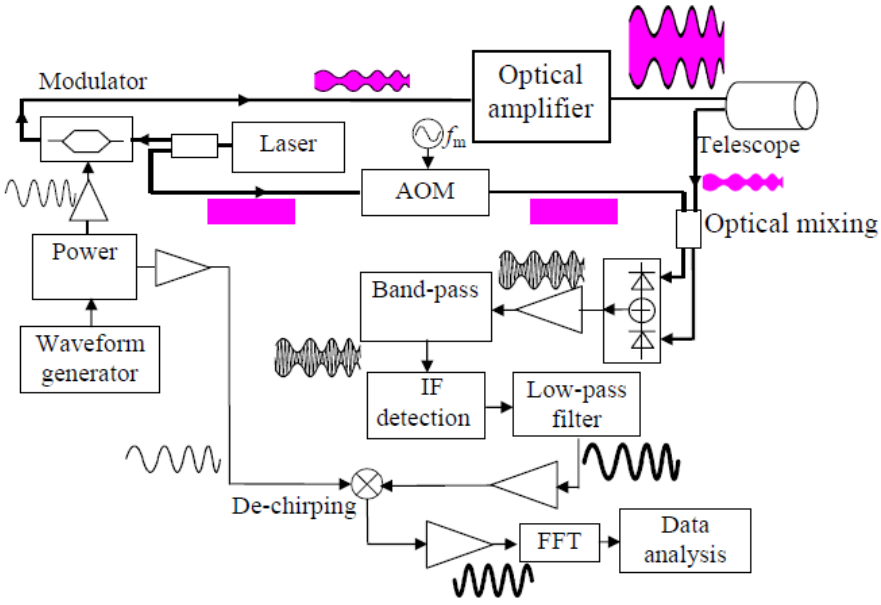

Fig. 2.6: Coherent heterodyne detection architecture [1].

2.3.3 Homodyne Self-Chirped Detection Architecture

The homodyne self-chirped architecture, shown in Fig. 2.7, was developed to maintain the receiver sensitivity obtained from coherent heterodyne detection while minimizing complexity. In this simplified homodyne detection scheme, the laser is modulated by the chirp waveform then split in two. One part of the modulated laser is amplified and sent out the telescope, the other is used as the LO. The returned laser signal is mixed with the LO via a 2x2 optical coupler the output of which is fed into a balanced photodetector. Because the LO is modulated with the same waveform as the transmitted laser, the optical mixing performs both optical detection and RF de-chirping. This reduces the amount of RF noise which is introduced to the detection signal. Performing an FFT on the output of the photodetector yields the beat frequency.

The simplification of the signal path in the homodyne self-chirped architecture results in a practical SNR closer to the theoretical SNR in (2.23) than the practical SNR of the coherent heterodyne architecture.

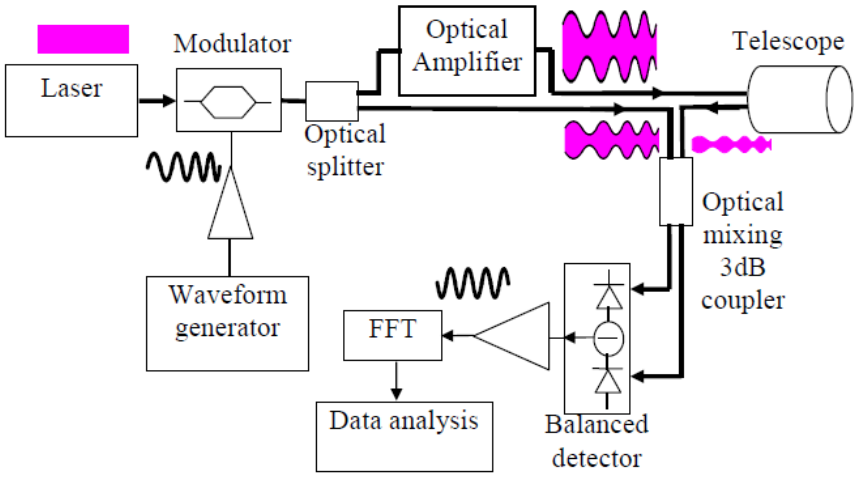

Fig. 2.7: Homodyne self-chirped detection architecture [1].

This architecture is popular for its performance and simplicity. Because it is being used by NASA for planetary landing missions [2–4, 11–13], it has been selected as the basis for the simulation being reported on in this thesis.

CHAPTER 3
LADARSIM MODIFICATION

3.1 LadarSIM Background

LadarSIM is a robust parameterized tool for simulating lidar systems, which has been developed at Utah State University's Center for Advanced Imaging Ladar (CAIL) since 2003 [5, 6]. LadarSIM was originally developed to simulated pulsed time-of-flight lidar systems and has the flexibility to simulate a wide range of these systems by simulating parameterized lidar transceiver, focal plane arrays, and pointing/scanning systems, as well as the interaction of the lidar with a simulated 3D scene.

3.1.1 Parameter GUIs

The main LadarSIM GUI is shown in Fig. 3.1. The GUI is split into three basic sections. The brown colored section in the center controls basic simulation parameters, such as scene selection, simulation fidelity, and what files the simulation will save.

The green section on the left side of the GUI is the geometry simulation. This section simulates the scenario from a strictly geometric standpoint. This simulation produces a point cloud using the scanner parameters, sensor flight path, and scene. The geometric simulation runs independently of the type of lidar to be simulated. The geometric measurements generated by the geometry simulation are used when LadarSIM simulates the actual performance of the specified lidar system.

The blue section on the right side of the GUI is the radiometric simulation. This cannot be run until after a geometric simulation of the scenario has been run. This side of the of the GUI can be used to simulate the performance of a particular lidar transceiver configuration. Parameters relating to the optical efficiency, transmitted beam, receiver, and range processing can be customized. The purpose of separating the geometric and

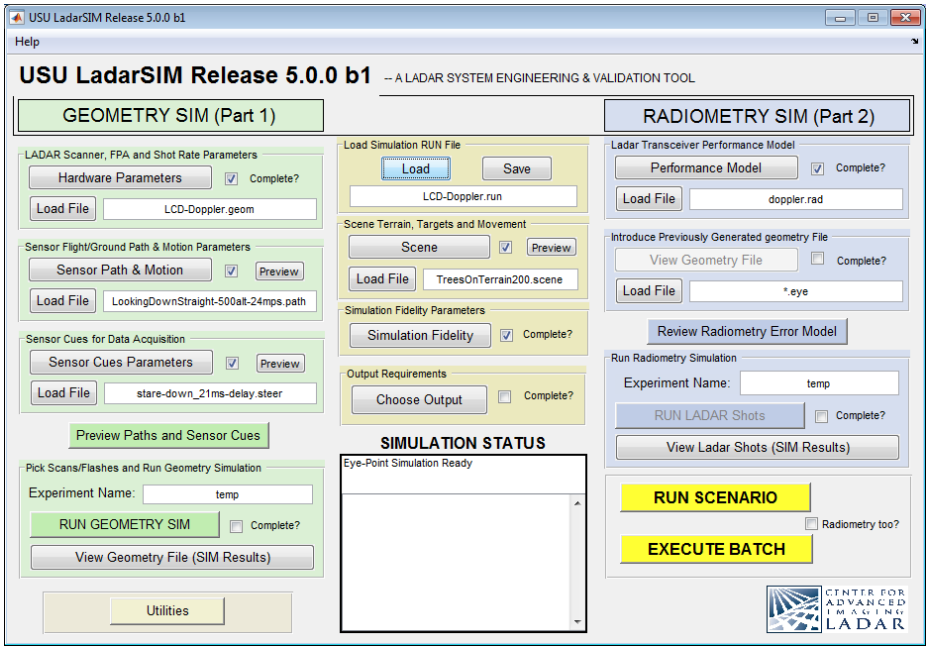

Fig. 3.1: Main GUI for running LadarSIM.

radiometric simulations is that the output of a single geometric simulation can be used to evaluate the performance of different lidar configurations.

3.2 Geometry Simulation Modification

The geometry simulation produces two useful items. The first is a point cloud of the scenario based only on the flight path, scanning parameters, and the scene. The second is what is called the "eyepoint file." This file contains measurements of the true range for each instance that the lidar would take a measurement based on the scanning parameters. This file can be saved for later use or passed directly to the radiometry simulation.

Before a simulation of Doppler lidar was added to LadarSIM, only time of flight (TOF) lidar was supported. In time of flight lidar, no direct measurement of velocity is taken so it was not necessary to include true measurements of radial velocity. The measure of radial velocity is, however, crucial to the simulation of a Doppler lidar system. For this reason the geometry simulation was modified to add radial velocity measurements to the eyepoint file.

3.3 Radiometry Simulation Modification

Because the transmit and receive processes are very different for TOF and FMCW lidar, more modification was necessary to the simulation of the radiometry simulation. Fig. 3.2 shows the "performance model" window. This is where parameters pertaining to the radiometry simulation are set. LadarSIM divides these parameters into four sections, optics, transmitter, receiver, and range processing. The parameters in these subcategories are different for TOF and FMCW lidar, the radio button pair marked "Instrument Type" selects which type of system is to be customized.

The Custom Optics GUI shown in Fig. 3.3 allows the user to specify the optical efficiency of the transmitter and receiver, the aperture diameter, and detector fill factor. These parameters are common between TOF and FMCW lidar so this GUI is used for both.

The Doppler Transmitter GUI is shown in Fig. 3.4. The user can use this GUI to set parameters related to the transmitted laser. Beam divergence, laser wavelength, and laser line width are important characteristics of the laser that have a large effect on the performance of the system. The "Temporal Pulse Shape" box allows users to specify the laser power and the chirp shape which has a direct effect on the capabilities of the system. Chirp bandwidth and length in time have a direct impact on the maximum resolution the system will be capable of, as explained in Section 2.1.

The "Receiver Parameters" GUI seen in Fig. 3.5 can be used to describe the electronics of the receiver. The behavior of the photo-diode is important because its bandwidth is leveraged directly by the homodyne self-chirped detection architecture discussed in Section 2.3.3. The gain and bandwidth of other analog receiver electronics can also be specified in this GUI.

Parameters directly related to range processing are set in the "Doppler Range Processing" GUI shown in Fig. 3.6. The threshold to noise ratio (TNR) dictates where the detection threshold should be set in relation to the noise and effects the probability of detection and false alarm. The maximum range and Doppler velocity the system is capable of resolving is dependent on the sample rate. The user can select to specify either the sample

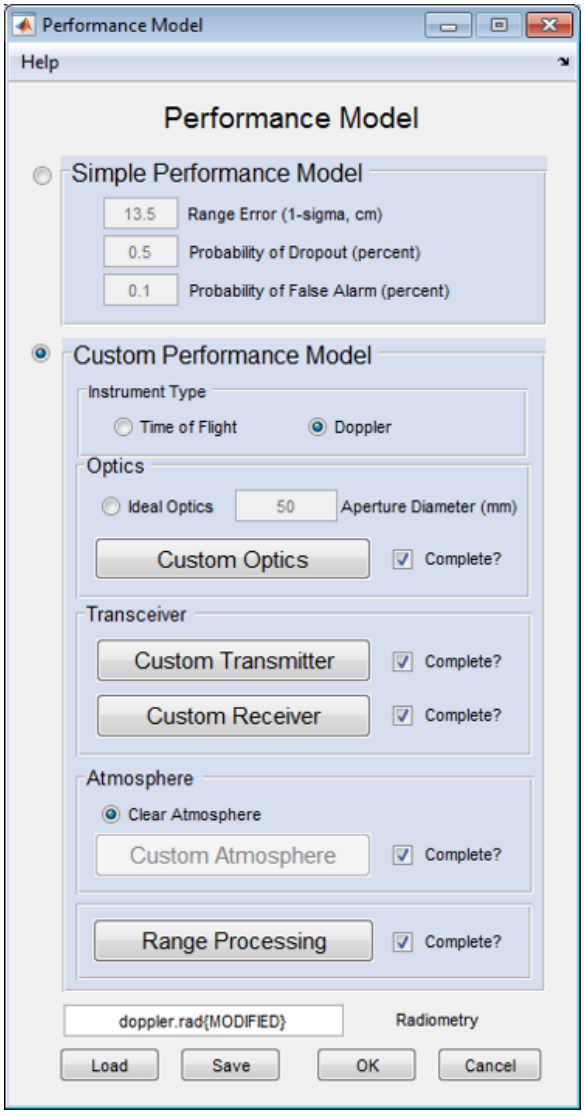

Fig. 3.2: Radiometry parameter GUI.

rate of the system or the maximum range at which the system is required to perform. The user must also specify the maximum velocity to be expected when the platform is at the maximum range. The best possible range resolution is determined by the chirp parameters (the theory behind this is described in Section 2.1). The user can then specify either the desired resolution or the size of the FFT used by the system to determine the other. The user can also specify what window to apply to the data.

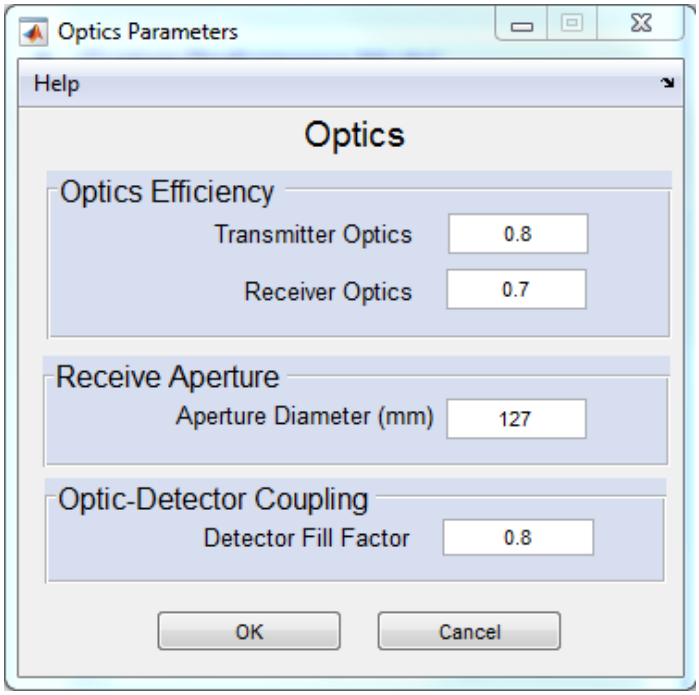

Fig. 3.3: Optical parameters GUI.

3.3.1 Simulation Process

After the geometry simulation has run and created an eyepoint file, the radiometric simulation can be run. Because LadarSIM runs the geometric simulation and the radiometric simulation separately, a user can run the geometric simulation once and use the output to compare the performance of several different lidar configurations. Section 3.1.1 explains how a user can configure the lidar to be simulated. LadarSIM is an engineering level simulation and does not simulate physical phenomena, such as atmospheric losses or the analog receiver circuitry, rather it approximates the effects of these processes [5,6]. The transceiver simulation can be divided into four stages.

First the laser transmitter is modeled. This includes parameters such as up-chirp and down-chirp frequencies and durations, transmitted laser power, local oscillator power, and various losses in the transmitter optics and alignment errors. To better simulate multiple targets in the beam footprint, non-uniform beam profiles, and sloped target surfaces, the beam footprint is sampled and each segment, or "beamlet", is modeled individually. The

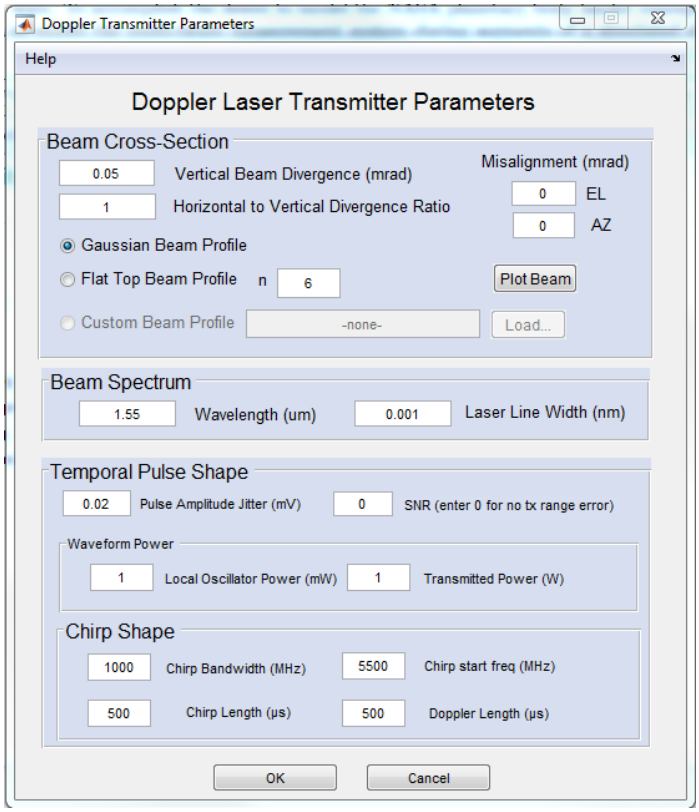

Fig. 3.4: Transmitter parameters GUI.

beam footprint covering a cliff edge or the edge of a boulder along with the ground below are two examples of what would cause multiple returns. The number of samples in the beam footprint can be specified depending on the desired simulation fidelity. Figure 3.7 shows a beam footprint with 109 beamlets. The beamlets are shown in green. A sloped surface or multiple targets in the beam footprint is a spread in the spectrum of f_b for the up-chirp and down-chirp segments and phase shifts in the returning energy of each beamlet at the f_d for the Doppler segment. Laser line width is also taken into account. LadarSIM assumes a Gaussian spectral shape for the line width [14]. A non-zero laser line width leads to a spread in the Doppler and the up-chirp and down-chrip spectra. Because the Doppler frequency (f_d) is directly related to the radial speed (v_r) and wavelength (λ),

$$f_d = \frac{2v_r}{\lambda}, \tag{3.1}$$

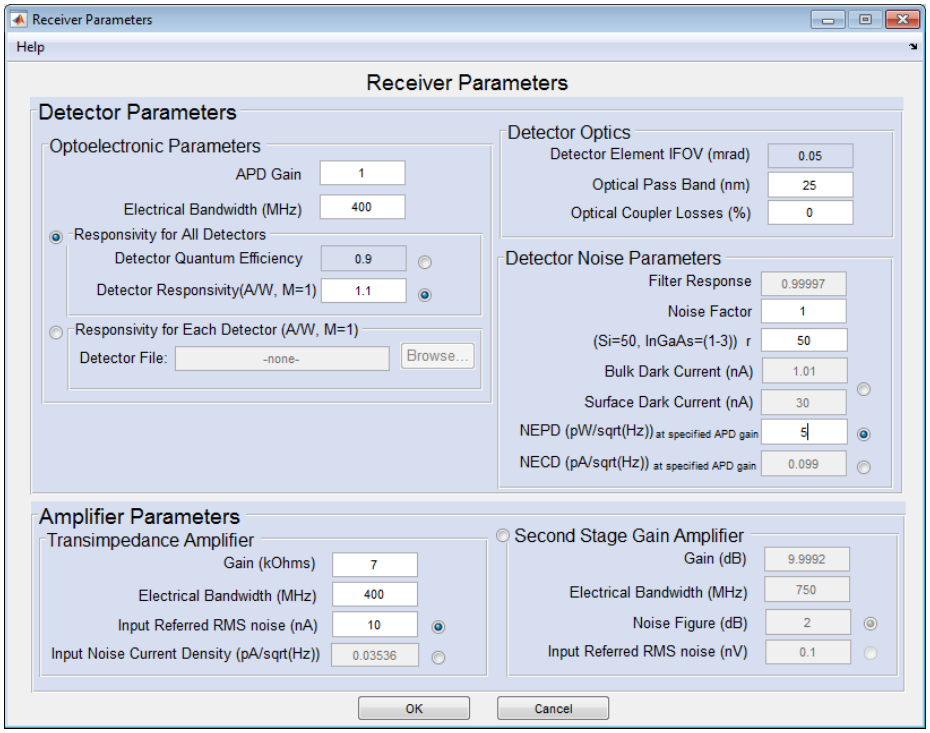

Fig. 3.5: Receiver parameters GUI.

as v_r increases the Doppler spectral spread increases.

The second stage of the transceiver simulation process determines the frequency, phase, and energy of the returning signal. Using the FMCW equations outlined in Chapter 2, the frequency, phase, and power for each beamlet in the beam footprint is determined. Then using a first order model to maintain a fast simulation, atmospheric backscatter and solar background radiation are applied. By processing each beamlet individually, this process accurately simulates the effects of multiple targets in the beam footprint as well as a sloped target surface.

After determining the returning frequency, phase, and power content of the returning signal, the third stage in the simulation process models the optical and analog receiver characteristics. The effects of the optocoupler, balanced photo detector, low-noise transimpedance amplifier, and optional additional amplification are condensed into one transfer function. This transfer function is applied to each beamlet to obtain the signal at the

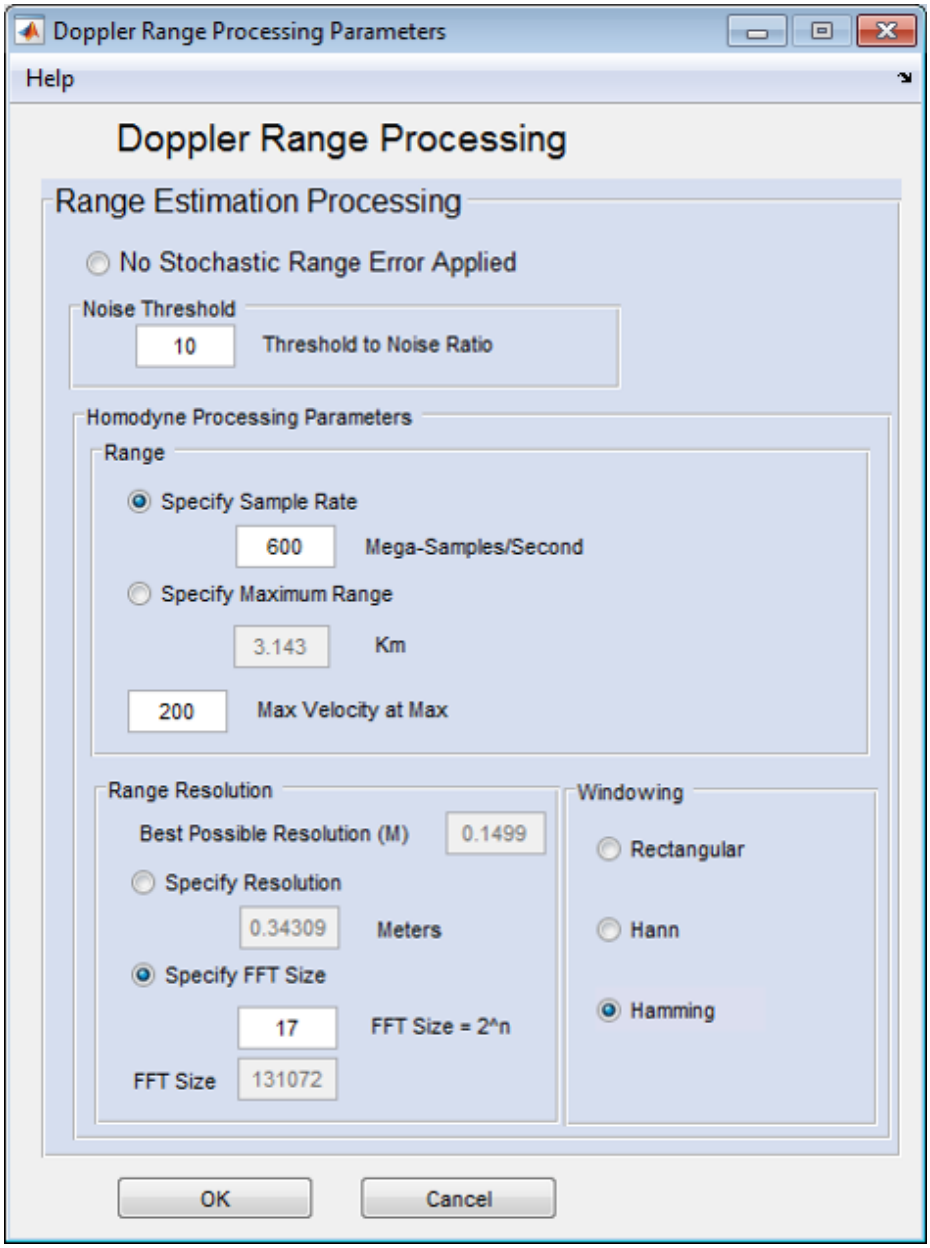

Fig. 3.6: Range processing parameters GUI

analog-to-digital converter (ADC).

The fourth and final step is to simulate the digital signal processing which is used to determine the range and radial speed of the targets within the beam footprint. LadarSIM

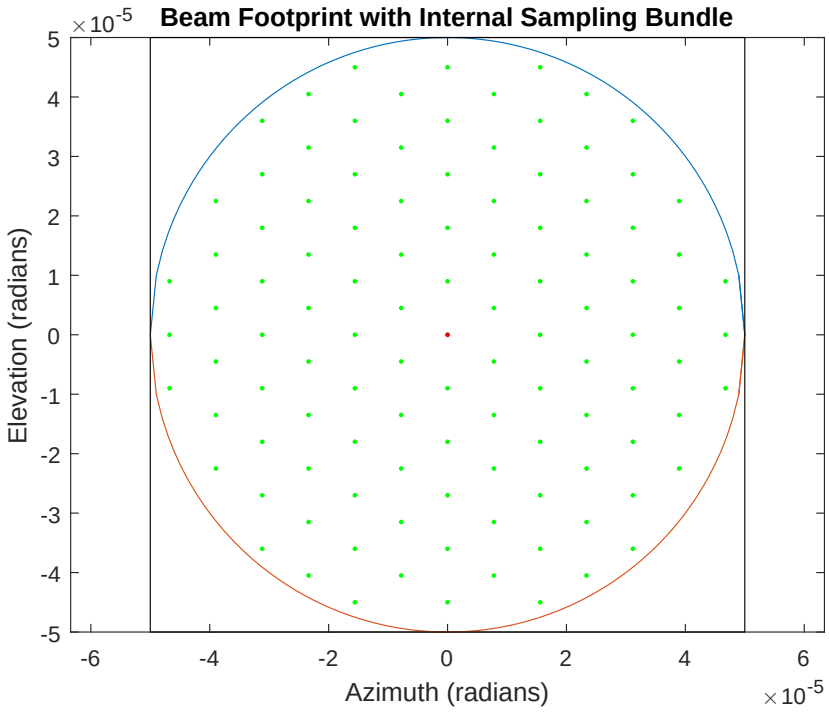

Fig. 3.7: Beam footprint with sampled beamlets.

attempts to make minimal assumptions about the signal processing techniques the lidar system will employ and therefore attempts to model the most straightforward detection algorithm. In a typical FMCW lidar system, an ADC digitizes the electrical signal produced by the analog detection circuitry. An FFT is then performed on the sampled signal and the bins of the FFT are used for the detection algorithm. The most straightforward way to simulate this process would be to generate a time domain signal based on the frequency, phase, and power content in the returning signal for each chirp segment and then to perform an FFT on each of the three segments. But because typical FFT sizes for an FMCW lidar are on the order of 2^{17}, and this must be performed for every chirp segment for every chirp this is computationally expensive and would result in a slow simulation. LadarSIM instead performs a simulation of that process which is much faster and includes the effects

of spectral leakage, spreading, and scalloping loss of the FFT.

The returning energy in an FMCW lidar will generally be contained within a narrow band of frequencies, in other words only a few of the FFT bins will have a non-zero or non-trivial magnitude. Knowing this, it is possible to obtain the magnitude in these bins without computing the entire FFT. LadarSIM does this by convolving the spectra of the mixed signals (as they would appear at the ADC) in the frequency domain with the frequency response of the user selected window function (rectangular, Hanning, or Hamming.) The signal spectrum is obtained by taking an FFT on the relatively narrow range of frequencies where the true spectra lie. The FFT required to perform this fast convolution is typically of size 2^{11} or 2^{12}. This process is done with much higher sampling rate in the frequency domain than the FFT bin spacing, then sampling the convolution output appropriately at frequency bin centers of the full-length FFT.

3.3.2 Probabilities of Detection and False Alarm

The simple detection algorithm employed by LadarSIM for FMCW detection finds groups of bins above the detection threshold and declares the bin with the largest magnitude in each group as a detection. A group may contain only one bin. Multiple groups occur when there are multiple targets in the beam footprint. LadarSIM does not directly add noise into the FFT bins to model the effects of noise in the system. Instead the probability that a detection will drop out and the probability that noise in a bin that does not contain a true return frequency will cause a false alarm are calculated. Then a random number is drawn and compared to these probabilities to determine if a detection drops out or if a false alarm occurs. The probability of detection is simply the probability that a detection is not dropped or the complement of the probability of drop out.

There are a number of phenomena which can cause noise in the signal. Shot noise is caused by the emission of photons in the laser. Solar background radiation is the ambient light which is sensed by the detector but is not related to the transmitted signal. Atmospheric backscatter noise is caused by light energy being reflected back by particles in the atmosphere. Electronic noise in the photo-detector and the analog amplification of the

electronic signal is also a factor [6]. These noise sources are combined to get an estimate of the power of the noise in the signal. The noise in the signal is then used determine the distribution of noise in an FFT which is a Ricean distribution if there is a non-zero signal in the bin and a Rayleigh distribution if the signal magnitude in the bin is zero. [15].

A drop out will occur when the signal magnitude in the peak bin of the FFT combined with the noise in that bin is less than the detection threshold. Because there is a non-zero magnitude in this bin, the noise distribution is Ricean. The Ricean parameter for a bin with magnitude $|X|$ is given by

$$\sigma^2_{|X|} = \frac{E_w \sigma_x^2}{2}, \tag{3.2}$$

where σ_x is the analog noise variance (including ADC noise), and E_w is the energy in the window function. The probability of detection is given by

$$P_d = Q_1\left(\frac{r}{\sigma_{|X|}}, \frac{Th}{\sigma_{|X|}}\right) \tag{3.3}$$

where Q_1 is the Marcum Q-function, r is the bin magnitude, and Th is the detection threshold, set by the user. Currently, LadarSIM uses the assumption that a detection must be found in both the up-chirp and the down-chirp segment FFTs in order to prevent a measurement dropout.

A false alarm occurs when a bin which does not correspond to a true detection frequency has a magnitude which is above the detection threshold. If the bin is near a true detection it may have energy from a sidelobe of the true detection peak. Otherwise it will have zero signal. If the bin has a non-zero signal the distribution of the noise in the bin is Ricean and the probability of false alarm is computed using (3.3). On the other hand, if the bin has zero signal magnitude the distribution of noise in that bin is given by the Rayleigh distribution. Hence the probability that noise alone will cause a bin to cross the detection threshold is given by

$$P_{faBin} = exp\left(-\frac{-Th^2}{2\sigma^2_{|X|}}\right). \tag{3.4}$$

Equation 3.4 gives the probability that a single bin will cause a false alarm. In an FMCW

detection process, any bin that is not part of or directly adjacent to a group of bins which is above the detection threshold can cause a false alarm. A bin directly adjacent to a group above the detection threshold cannot cause a false alarm because if it is above the detection threshold it will not cause a new detection although it could potentially cause an error in the measurement if its magnitude were the largest in the group. The total probability of false alarm is therefore the probability that a false alarm occurs in any of the bins described.

Because the spectral energy detected in a typical FMCW process is very tightly packed, there are only a few bins which are exempt from the possibility of causing a false alarm. The total probability of false alarm is a similar to the probability that when many dice are rolled at least one of them rolls a six. For a single die the probability that a six will be rolled is $\frac{1}{6}$. If six dice are rolled the probability that at least one six will be rolled is not

$$P_{six} \neq \frac{1}{6} + \frac{1}{6} + \frac{1}{6} + \frac{1}{6} + \frac{1}{6} + \frac{1}{6} = 1. \tag{3.5}$$

It is given by the complement of the probability that no sixes will be rolled:

$$P_{six} = 1 - (\frac{5}{6})^6 = 0.6651. \tag{3.6}$$

Where the probability that a single die will not roll a six is $\frac{5}{6}$. So the probability that at least one bin causes a false alarm is the complement of the probability that no bins cause a false alarm:

$$P_{fa} = 1 - (1 - P_{faBin})^{2^{N_{FFT}-M}}, \tag{3.7}$$

where N_{FFT} is the size of the FFT and M is the number of bins with some signal associated with a true detection.

The probabilities of detection and false alarm are used to determine if a shot is detected or whether a false alarm occurs. Once the spectra are obtained for each chirp segment of a lidar shot and the probabilities of detection and false alarm are determined, a uniform random number is then drawn for each event to determine if that event occurs. For a missed detection, that point is simply excluded from the point cloud. For a false alarm, a false

peak is placed in a randomly selected FFT bin before detection processing occurs.

3.4 Example Point Clouds

FMCW Doppler lidar is commonly used to determine relative position and obtain a velocity vector of the platform on which the lidar is mounted. This can be done by taking three measurements at different angles from the craft. NASA uses an FMCW lidar in this way on their Morpheus test vehicle [2–4]. This configuration uses three lidar transmitters with three fixed telescopes making a 45° cone angle. This configuration provides sufficient information to obtain a velocity vector and an estimate of the altitude of the craft. This lidar configuration and novel alternatives are simulated and compared in Chapter 5. In this section, the capabilities of LadarSIM's FMCW Doppler lidar simulation will be demonstrated by showing point clouds and detection spectra produced for a lidar configuration which produces a much denser point cloud.

In this scenario, an FMCW Doppler lidar is flown at an altitude of 250 m above a 3D scene. The terrain is hilly with a small group of trees in the center. The lidar is configured with two beams, one pointed slightly forward at an angle 250 μrad less than perpendicular to the flight path and the other slightly back at an angle of 250 μrad past perpendicular. The beams scan from side to side across the scene below the moving platform. As the lidar moves forward the radial velocity measured by the forward beam will have a small positive magnitude and the beam pointed backward will have a small negative magnitude. The results of this simulation are shown in Fig. 3.8.

Figure 3.8(a) shows an example set of return spectra. The top spectrum represents the range frequency spectrum and the bottom, the Doppler frequency spectrum. The green dotted line is the detection threshold, the red dotted line is the power of the noise in the system, and detection frequencies are shown in maroon. The two peaks in the range spectrum are a result of part of the beam footprint hitting a leaf and the remainder hitting the ground below the tree. There is only one detected radial velocity because the platform is moving at the same radial velocity in relation to the leaf and the ground.

Figures 3.8(b) and 3.8(c) show the point cloud generated by this experiment colored by

range and radial velocity respectively. In Fig. 3.8(c), alternating red and blue points can be seen. Pairs of these points correspond to the forward and backward pointed beams which measure a slight positive and slight negative velocity respectively. Note that the points in both Fig. 3.8(b) and 3.8(c) are located in distinct layers. This is a consequence of the discrete nature of the FFT, the ranges are quantized by the discrete bin values of the FFT.

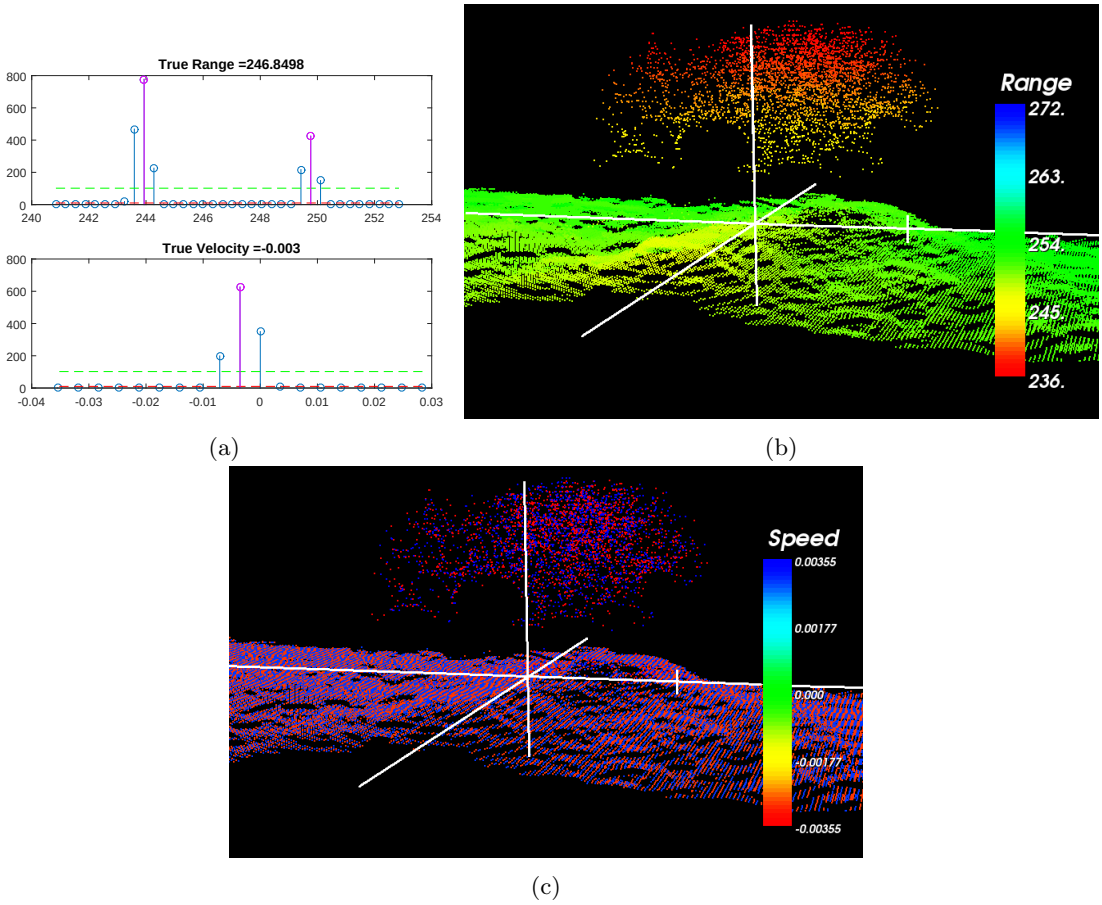

(a) (b)

(c)

Fig. 3.8: Simulation results for the dense point cloud scenario. The cross hairs point to an arbitrary point near the center of the cloud. The axes of the cross hairs have the same scaling and the tic is approximately 10 m from the cross hair origin. (a) FFT bin values for measurement with two returns. The green dashed line represents the detection threshold, the red dashed line is the noise variance, and the maroon points are the detected measurements. A Hamming window was used. (b) Point cloud colored by range in meters. (c) Point cloud colored by velocity in meters per second.

CHAPTER 4
FMCW LIDAR PERFORMANCE

4.1 Overview

This chapter presents the results of a study of the probability of detection and false alarm using the LadarSIM FMCW Doppler lidar simulation. Instead of using LadarSIM to create point clouds of many different scenarios with various lidar configuration then using the Monte Carlo method to determine probabilities of detection and false alarm, this study used LadarSIM's Error Model Review GUI, shown in Fig. 4.1. This GUI allows a user to specify the range to target, speed in the direction of the target, and the anglfe of incidence to the target, which is a flat plane with user specified reflectivity. LadarSIM will then calculate noise in the system, probability of detection, and probability of false alarm. By clicking the "Plot Trial Signal" button, the user can generate the detection spectra for that shot and receive a report of the detected range and radial velocity. Figure 4.2 shows the detection spectra and the detection report generated for the parameters specified in Fig. 4.1.

To perform a thorough study of the performance of an FMCW lidar by manually entering in values would be very tedious and subject to human error. The Error Model Review GUI was modified to improve the process of gathering detection and false alarm statistics. A user can now create a file which specifies which experiments are to be performed and load it by clicking the "Run Trial" button and LadarSIM will run the experiments and output the detection and false alarm statistics to a file for later use. The output file can then be used to generate plots which show the performance of lidar configurations over various ranges and angles of incidence.

The rest of this chapter will present results of experiments which were performed using the modified Error Model Review GUI. All simulation parameters, unless otherwise noted, are given in Table 4.1.

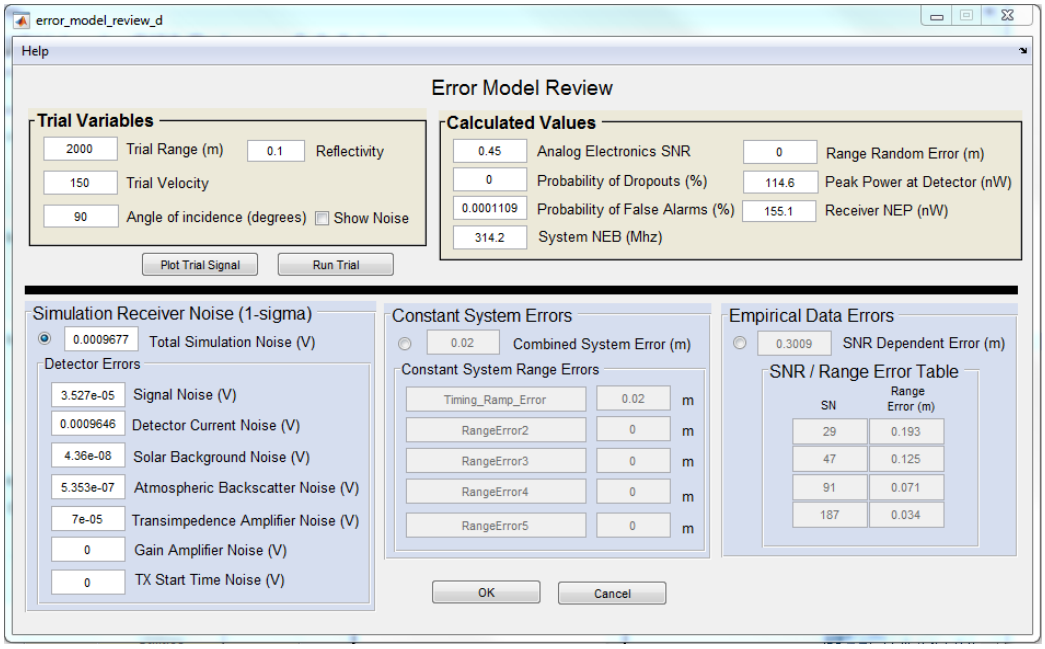

Fig. 4.1: GUI for simulating single shots.

Table 4.1: Parameters for every simulation unless otherwise noted.

Common Simulation Parameters		
Transmitter/Receiver	Aperture	25 mm
	Wavelength	1550 nm
	Transmitted Power	1 W
	Local Oscillator Power	1 mW
	Chirp Bandwidth (B)	1 GHz
	Chirp Start Frequency (F_1)	5.5 GHz
	Chirp Length (T)	500 μs
	Beam Divergence	50 μRad
Detector	APD Gain	1 (pin diode)
	Electrical Bandwidth	400 MHz
	Responsivity	1.1 A/W
	Optical Passband	25 nm
	NEPD	5 pW/$\sqrt{\text{Hz}}$
Transimpedance Amplifier	Transimpedance Gain	7 kΩ
	Electrical Bandwidth	400 MHz
	Input Referred RMS Noise	25 nA
Range Processing	Sample Rate	600 MHz
	FFT Size	2^{17}
	Window Type	Hamming

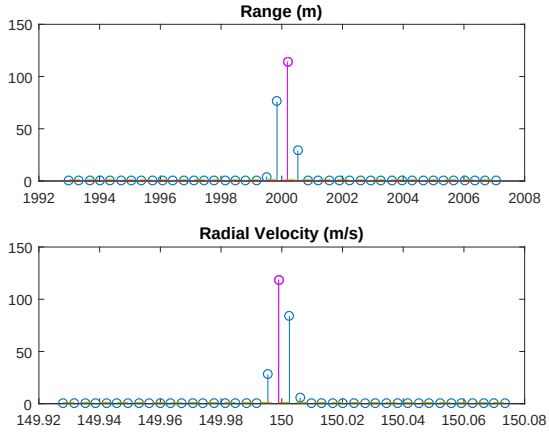

(a)

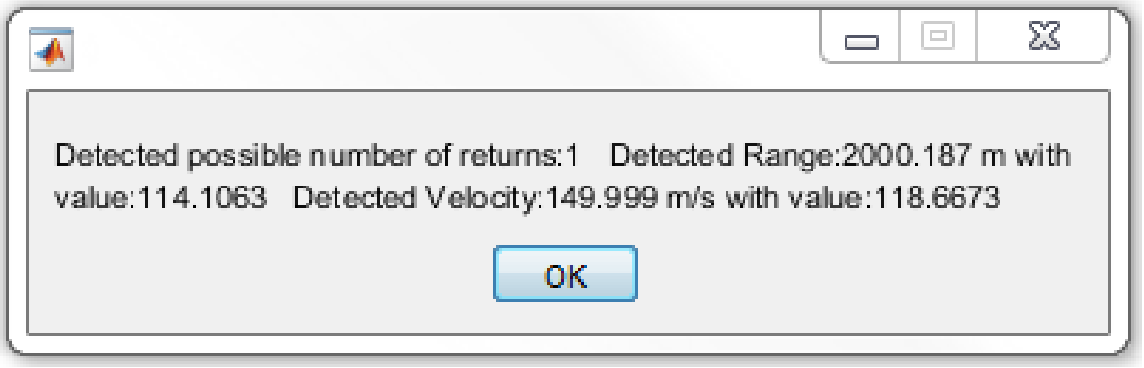

(b)

Fig. 4.2: Simulation results for a target at 2000 m with 150 m/s velocity. (a) Detection spectra. (b) Detection report.

4.2 Range and Angle of Incidence

The range to target and the angle at which the laser impinges on the target both have effects on the performance of an FMCW lidar. Both effects stem largely from imperfect beam divergence. An ideal (non-diffraction limited) laser beam would have zero divergence, i.e. the beam width would not spread out over a distance; due to diffraction there is always some non-zero beam divergence. A laser in an FMCW Doppler lidar might have a beam divergence of 0.5 mrad. This beam divergence will cause the beam diameter to be 1 m at a distance of 2 km. Laser power is related to range by the inverse square law. Laser power

(S) is related to the range (R) proportionally:

$$S \propto \frac{1}{R^2}. \tag{4.1}$$

Because the laser must travel to the target and back, the target echo power (S_r) is related to the range by

$$S_r \propto \frac{1}{(2R)^2}. \tag{4.2}$$

Beam divergence causes the laser energy to be spread across the beam footprint. Because each point in the beam footprint is at a slightly different range from the lidar, the energy reflected by disparate parts of the beam footprint will vary in beat frequency f_r and have different phases of the Doppler frequency f_d. This spectral spreading is amplified when the surface is not perpendicular to the impinging laser. The up-chirp and down-chirp segments are primarily affected by the spreading of energy across several frequencies as the angle varies. The Doppler segment is subject to constructive and destructive interference because the returning energy is at the same frequency, f_d, but spread out in phase. This leads to more intermittent performance of the Doppler segment than the up- and down-chirp segments. Figure 4.3 shows the detection spectra for a range of 2000 m, a radial velocity of 10 m/s, and angles of incidence of 90° and 45°. A significant decrease in magnitude of the peak in the FFT can be observed between the 90° case and the 45° case for both the range detection, which corresponds to the up- and down-chirp segments, and the radial velocity detection corresponding to the Doppler segment, although the decrease is slightly greater for the Doppler segment.

Because of the decreased intensity due to range and the spectral spreading from the angle of incidence, the performance of an FMCW Doppler lidar is dependent on both range and angle of incidence to the target. Figure 4.4 shows the results of an experiment in which the range was varied from 1 to 10,000 m and the angle of incidence was varied from 1° to 90°. Figure 4.4(a) shows the probability of detection for the up- and down-chirp segments over the ranges and angles of incidence and Fig. 4.4(b) shows the same for the Doppler segment.

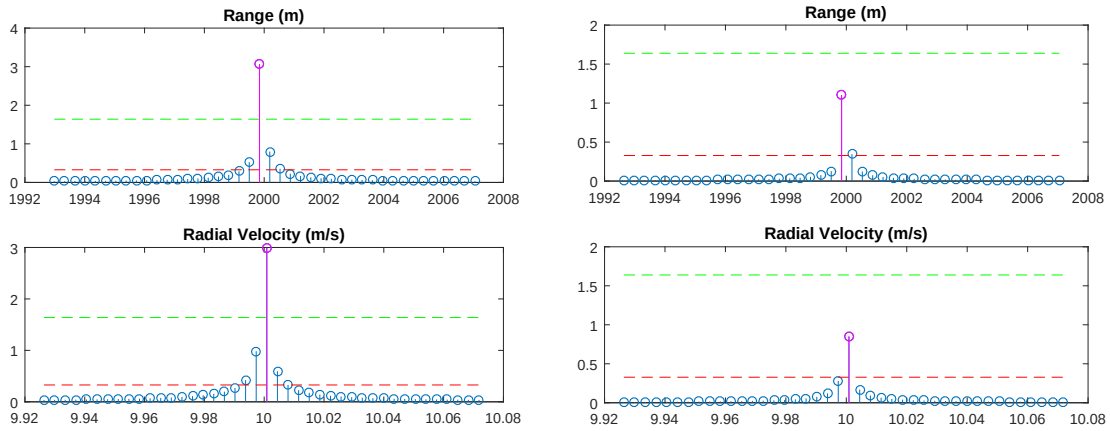

(a) (b)

Fig. 4.3: Simulation results for a target at 2000 m with 10 m/s velocity using rectangular windowing and a 1 mrad beam divergence (a) 90° angle of incidence. (b) 45° angle of incidence.

For the up- and down-chirp segments the probability of detection is high in the large yellow region. Dropouts occur frequently at low angles and as the range increases the upper limit of these low angles increases. There also begin to be dips and valleys of low probability of detection at higher angles at higher ranges. These are caused by the combination of sidelobe interference between the spread out detection frequencies and scalloping loss.

Scalloping loss is a phenomenon of the FFT which is sometimes referred to as the picket fence effect. This is because looking at magnitude the FFT bins of a signal can be thought of as looking at a mountain range through a picket fence. The spaces between slats of the fence reveal glimpses of the mountain range. If the peak of a mountain is hidden behind a slat the highest points observed are in the spaces at either side of that slat. These observed points could potentially be much lower than the actual peak of the mountain. Similarly, if the peak frequency in a signal is not aligned with a bin frequency in the FFT, the energy in the bins at either side of the frequency, the magnitude in those bins will be less than the actual magnitude of that frequency. This can cause higher probability of dropout when the signal power is near the detection threshold and the beat frequency is not aligned with a bin

center leading to rapidly fluctuating performance with respect to small changes in range or angle of incidence at longer ranges (for the lidar simulated in Fig. 4.4(a) above about 4000 m.)

The surface plot in Fig. 4.4(b) is shown looking straight down to allow better visibility of the effects on the Doppler segment. The curved lines of low detection probability are a result of destructive interference caused by the phase shifted signals from different parts of the beam footprint. The fact that those curves are dashed comes from scalloping loss.

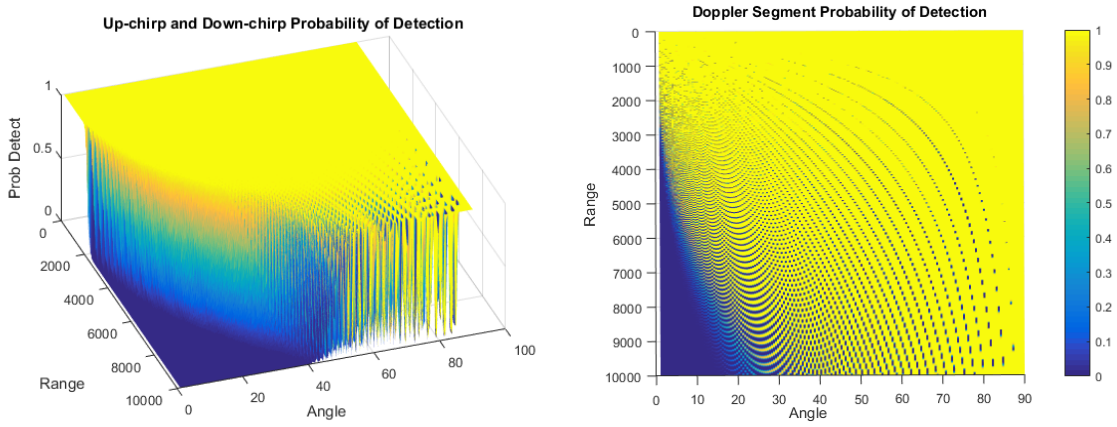

(a) (b)

Fig. 4.4: Simulation results for ranges from 1 to 10,000 m and angles 1° to 90°. (a) Probability of detection for the up-chirp and down-chirp segments. (b) Probability of detection for the Doppler segment. (Surface shown from above to make all dips visible.)

The probability of false alarm is a function of the noise in the system. The noise in the system is mostly unrelated to the range and angle to target. The exception being at very close ranges, i.e. under about 5 m, where the power of the returning light is relatively high. Although this leads to a high signal to noise ratio (SNR), the magnitude of the noise is still higher than in the rest of the regime of operation. In a detection process where the magnitude in an FFT bin simply must exceed the detection threshold, this will lead to a higher rate of false alarm. Outside of this close range, the probability of false alarm varies

only slightly across changes in range and angle. Therefore, the probabilities of false alarm presented in the remainder of this chapter will be the average probability of false alarm for ranges greater than 5 m.

4.3 Threshold

The detection threshold determines the magnitude an FFT bin must contain to be considered a detected signal. A lower threshold allows lower power returns to be detected but also allows lower noise to cause false alarms. Thus any increase in detection probability gained by lowering the detection threshold is a trade off which leads to an increase in the probability of false alarm. LadarSIM uses a threshold to noise ratio (TNR) to determine the detection threshold. Typically a receiver operating characteristic curve (ROC curve) is used to demonstrate the this trade off, however; because the detection probability for FMCW Doppler lidar is so closely tied to range and angle of incidence it is difficult to choose a range and angle of incidence at which to create a ROC curve. Instead Fig. 4.5 shows the probabilities of detection for the same lidar configuration with TNRs of 1, 5, 10, and 15 and Table 4.2 shows the corresponding per-bin false alarm probabilities.

Notice how the blue triangular area of near zero probability for low angles and longer ranges grows as the threshold is increased. The depth and number of valleys and dips of low detection probability also increases with the TNR. Figure 4.5(a) shows that when the TNR is one, there is a very high probability of detection over nearly the entire regime but the per-bin probability of false alarm is 0.8 as shown in Table 4.2. Using (3.7) and substituting in $P_{faBin} = 0.8$ yields a total probability of false alarm very close to one. On the other hand the probability of false alarm for a TNR of 15 is very low, but Fig. 4.5(d) shows that this comes at the expense of performance at low angles and long ranges. The TNR of 10 provides a reasonable false alarm rate and a large regime of good probability of detection the results of which are shown in Fig. 4.5(c).

4.4 Trade-offs

In this section the results of a trade-off study using the updated LadarSIM are shown. The results of these experiments will be informative in the process of designing or selecting an FMCW lidar to meet mission requirements. The laser transmission power and aperture diameter were selected because of their effect on the ranges and angles at which an FMCW lidar will perform well. FFT size was included in this tradeoff study because of its effect

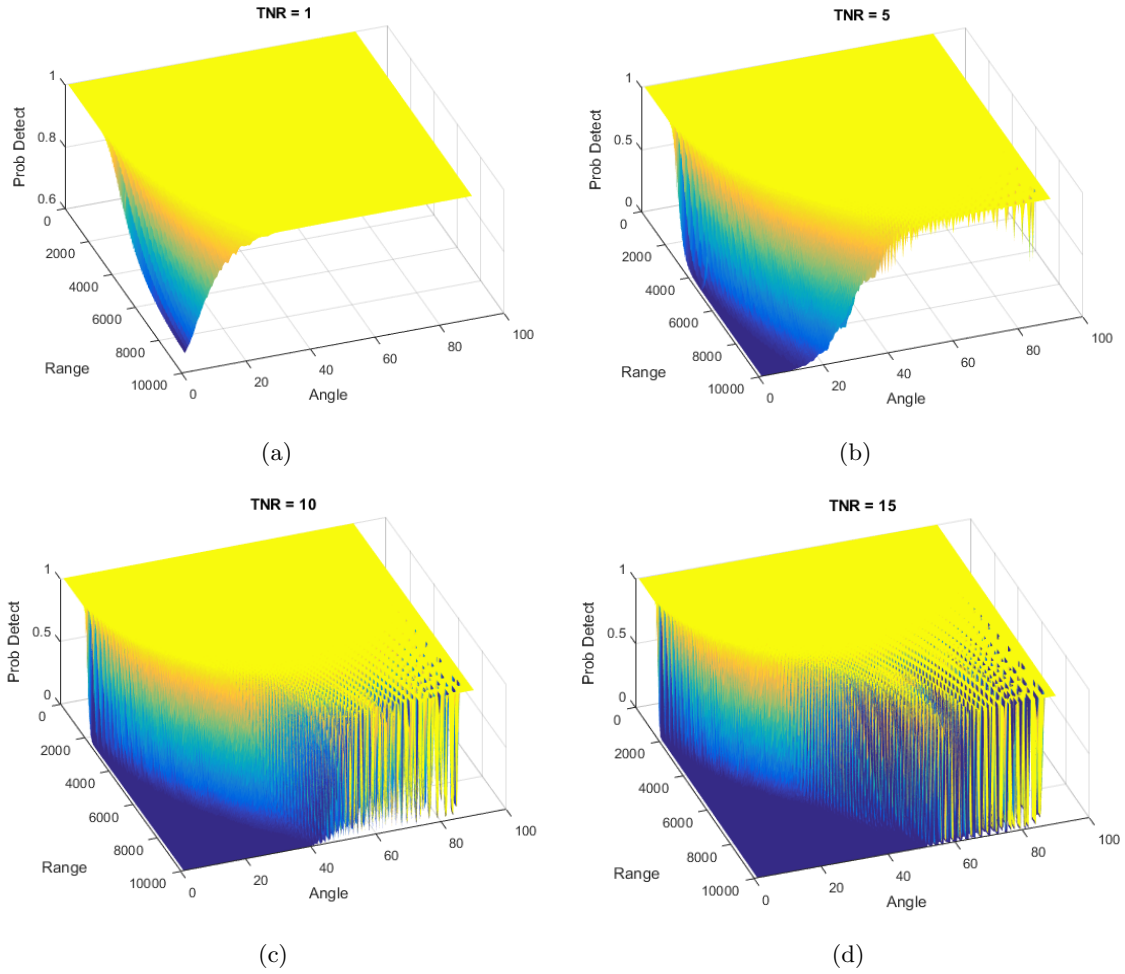

Fig. 4.5: Probability of detection simulation results for ranges from 1 to 10,000 m and angles 1° to 90° using a Hamming window. (a) Threshold to noise = 1. (b) Threshold to noise = 5. (c) Threshold to noise = 10. (d) Threshold to noise = 15.

Table 4.2: Per-bin false alarm rates for varying threshold to noise ratios.

TNR	PFA/bin
1	0.8
5	0.047
10	5.06e-10
15	1.17e-21

on computational requirements and thus power consumption of the system and, because of scalloping loss, the FFT size also has an effect on dips and valleys of detection probability like the ones seen in Fig. 4.4(a). In this section, the effects of these three parameters on

performance are shown and discussed but the associated cost in weight, power consumption, financial cost of the system etc. are beyond the scope of the research.

Three experiments were performed for each trade-off parameter and the probabilities of detection and average probability of alarm recorded. First, the range was varied from 5 to 10,000 m with the angle of incidence fixed at 15°, second, the range was varied from 5 to 10,000 m with the angle fixed at 85°, and finally, the range was fixed at 3500 m and the angle of incidence varied from 1° to 90°. Each of these experiments can be thought of as taking a slice of a probability of detection surface like the ones shown in Fig. 4.4(a). This was favored over a surface because it is easier to directly compare different values of the trade-off parameter with these slices. It should be noted that all experiments which correspond to a transmitted power of 1 watt, an aperture diameter of 25 mm, and an FFT size of 2^{17} are identical as made clear by Table 4.1.

4.4.1 Transmission Power

Transmission power is the power of the laser radiation which exits the instrument to illuminate the target. The most obvious way to increase the detection range limitation described by (4.1) is to increase the transmission power. A more powerful laser will improve the probability of detection at longer ranges but will consume more power from the system and may weigh and cost more than a lower power laser.

Figure 4.6 shows the experiments for the transmission power trade-off. Figure 4.6(a) shows the results for the angle of incidence held fixed at 15°, Fig. 4.6(b) shows the results for the angle of incidence held fixed at 85°, Fig. 4.6(c) shows the results for the range fixed at 3500 m. Figure 4.6(a) shows that as the transmission power is increased the range at which a shot with an angle of incidence of 15° can be detected increases. The dip in probability of detection for the 1 watt laser shown in Fig. 4.6(b) correlates to a valley like the ones seen in Fig. 4.4(a). As the transmitted power is increased, the effects that lead to lower detection probability in this valley are overcome. Figure 4.6(c) shows that lidar systems with higher transmission power are able to detect shots with lower angles of incidence. Table 4.3 shows the average probability of false alarm for each experiment with each lidar configuration. The

benefits of increasing transmission power come at the cost of a small increased probability of false alarm.

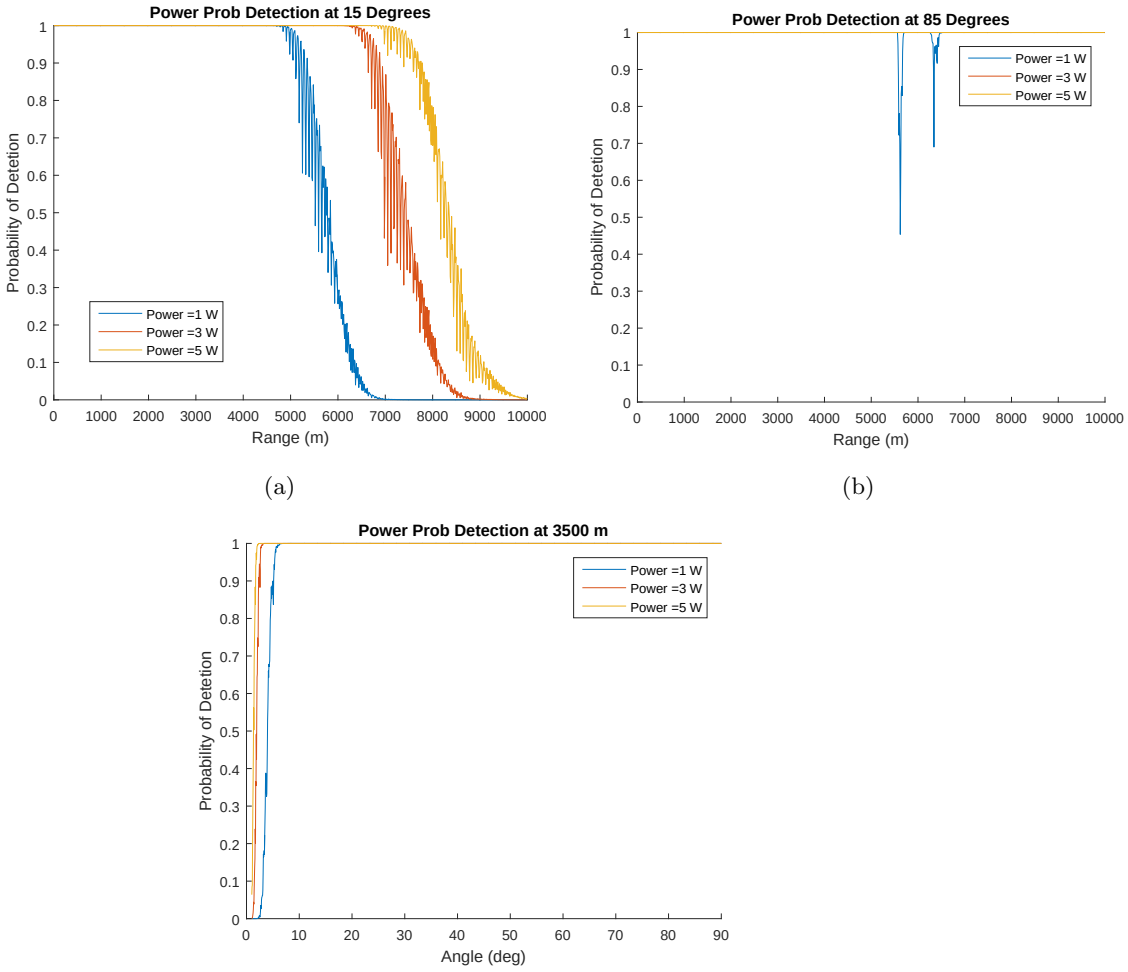

Fig. 4.6: Comparison of performance of 1, 3, and 5 watt laser powers. (a) Range varied from 5 to 10,000 m angle fixed at 15°. (b) Range varied from 5 to 10,000 m angle fixed at 85°. (c) Angle varied from 1° to 90° range fixed at 3500 m.

Table 4.3: False alarm rates for varying transmission power for the experiments shown in Fig. 4.6.

Power	15° PFA	85° PFA	3500 m PFA
1 W	0.445e-8	0.431e-8	0.425e-8
3 W	0.488e-8	0.448e-8	0.437e-8
5 W	0.534e-8	0.462e-8	0.445e-8

4.4.2 Aperture Diameter

The aperture diameter is the size of the opening through which the returning laser is received. The aperture diameter restricts how much returning light is captured by the lidar having a direct effect on its ability to detect. Doubling the area of the aperture allows twice as much returning laser energy to be received. LadarSIM assumes a circular aperture giving an area A of

$$A = \pi(\frac{D_{ap}}{2})^2, \tag{4.3}$$

where D_{ap} is the aperture diameter. It is clear from (4.3) that doubling the aperture diameter leads to four times as much laser energy to be received.

Figure 4.7(a) shows the the aperture diameter trade-off experiment with the angle of incidence fixed at 15° while varying the range. Here it is clear that with larger aperture diameters the range the lidar is able to detect at 15° increases. Figure 4.7(b) shows that the effects of the dips and valleys of detection probability are mitigated with a larger aperture diameter. The minimum angle at which the lidar can detect a shot decreases as the aperture diameter is increased as shown in Fig. 4.7(c). The false alarm rates shown in Table 4.4 show that with an increase of aperture diameter comes a small increase in the false alarm rate. This is because the noise in the system increases with the magnitude of returning power. Comparing the experiments in Fig. 4.7 to those in Fig. 4.6 it is clear that increasing aperture diameter has a similar effect on the performance of the system to an increase in transmission power. This is expected from the lidar range equation, given by

$$S = \frac{PA\tau_o\rho}{2\pi R^2}, \tag{4.4}$$

where S is the target echo power at the receiver, P is the transmitted power, A is the area of the aperture, τ_o is the optical efficiency of the system, and R is the range.

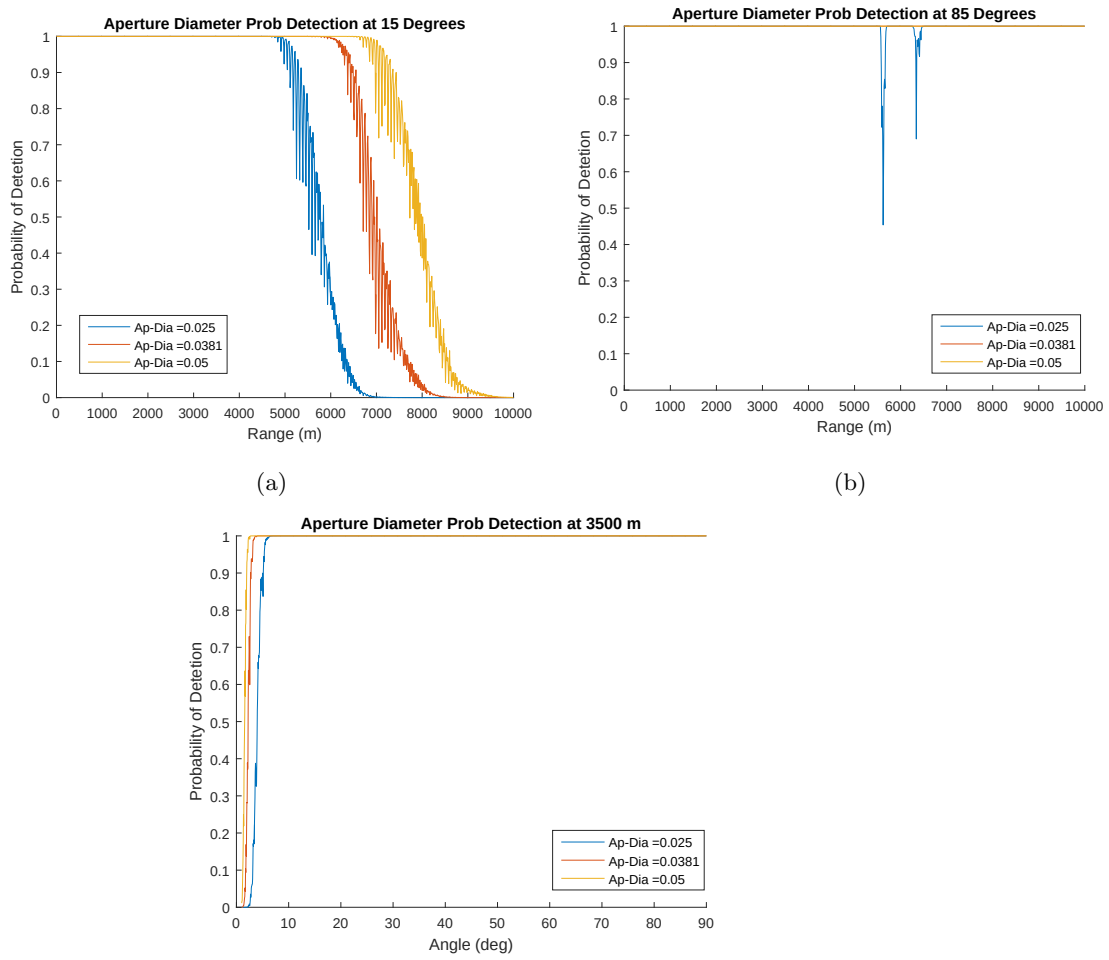

Fig. 4.7: Comparison of performance of 25, 38.1, and 50 mm aperture diameters. (a) Range varied from 5 to 10,000 m angle fixed at 15°. (b) Range varied from 5 to 10,000 m angle fixed at 85°. (c) Angle varied from 1° to 90° range fixed at 3500 m.

Table 4.4: False alarm rates for varying aperture diameters for the experiments shown in Fig. 4.7.

Aperture	15° PFA	85° PFA	3500 m PFA
25 mm	0.445e-8	0.431e-8	0.425e-8
38.1 mm	0.474e-8	0.443e-8	0.433e-8
50 mm	0.511e-8	0.456e-8	0.441e-8

4.4.3 FFT Size

The same experiments that were performed for transmission power and aperture diameter were performed by varying the FFT size while holding transmission power and aperture diameter constant. The results are shown in Fig. 4.8 and Table 4.5. The size of the FFT is almost always a base two number because of the availability of radix two FFT libraries and FPGA cores. The computational complexity of an FFT of length n is given by

$$O(nlog(n)). \tag{4.5}$$

The relative complexity of a system which uses a 2^{18} point FFT versus a system using a 2^{17} FFT is

$$\frac{2^{18}log(2^{18})}{2^{17}log(2^{17})} = 2.1176. \tag{4.6}$$

This approximate doubling of computational requirements will result in added power consumption of the processor or FPGA.

The bin spacing of an FFT is the distance in frequency between the bins of the FFT. Given the number of bins in the FFT (which is the same as the size of the FFT) and the sample rate, the bin spacing can be calculated by

$$f_{bin} = \frac{f_n}{N_{bins}}, \tag{4.7}$$

where f_n is the sample rate. Because range and radial velocity are detected from the frequency bins of the FFT, the bin spacing limits the resolution of the system. The resolution is also limited by the chirp bandwidth as explained in Section 2.1.2. The resolution in range can be determined by substituting f_{bin} from (4.7) into (2.10) for δf. The resolution in radial velocity can be obtained similarly by substituting f_{bin} for the Doppler frequency in (2.21).

A less obvious consequence of the FFT size is the periodic degradation of the probability of detection caused by scalloping loss [16]. This can be seen in Fig. 4.8. Note the frequent dips on the curves corresponding to an FFT size of 2^{16}. These dips become less severe with increased FFT size. From the results of the simulation increasing the size of the FFT in

the system may not significantly increase the regime of performance but will mitigate or prevent dead spots caused by scalloping loss. Increasing the size of the FFT increases the probability of false alarm as shown in Table 4.5. This is largely due to the increase in the number of bins which have the potential to cause a false alarm and could be mitigated by a detection algorithm which rejects detections outside of an expected range.

4.5 Discussion

It should be noted that the curves in Figs. 4.6, 4.7, and 4.8, which correspond to 1 watt transmission power, 25 mm aperture diameter, and a 2^{17} FFT respectively, are identical as made clear by Table 4.1.

An increase in transmission power or aperture diameter have similar effects. This relationship is evidenced by the similarities between Figs. 4.6 and 4.7. This is because a larger aperture creates a larger area to capture light leading to larger return power. Obviously a larger transmitted power leads to more return power. This relationship is useful to note. If a system has a constraint on transmission power or aperture diameter, increased performance can be obtained by adjusting the unconstrained parameter. Because of scalloping loss, the FFT size has an effect on probability of detection. This should be taken into account in the design of an FMCW lidar system.

In designing an FMCW lidar system, it is important to take into consideration not only the distances at which the system is expected to operate but the expected angles of incidence at a long range. For example, a lidar on a lander coming in at a shallow angle at a high altitude might not perform as well as expected because of a low angle of incidence to the ground at a long range. It may also be important to take into consideration the presence of the valleys of detection probability at certain angles at longer ranges as seen in Fig. 4.4(a) if performance in the regime where these valleys exist is mission critical.

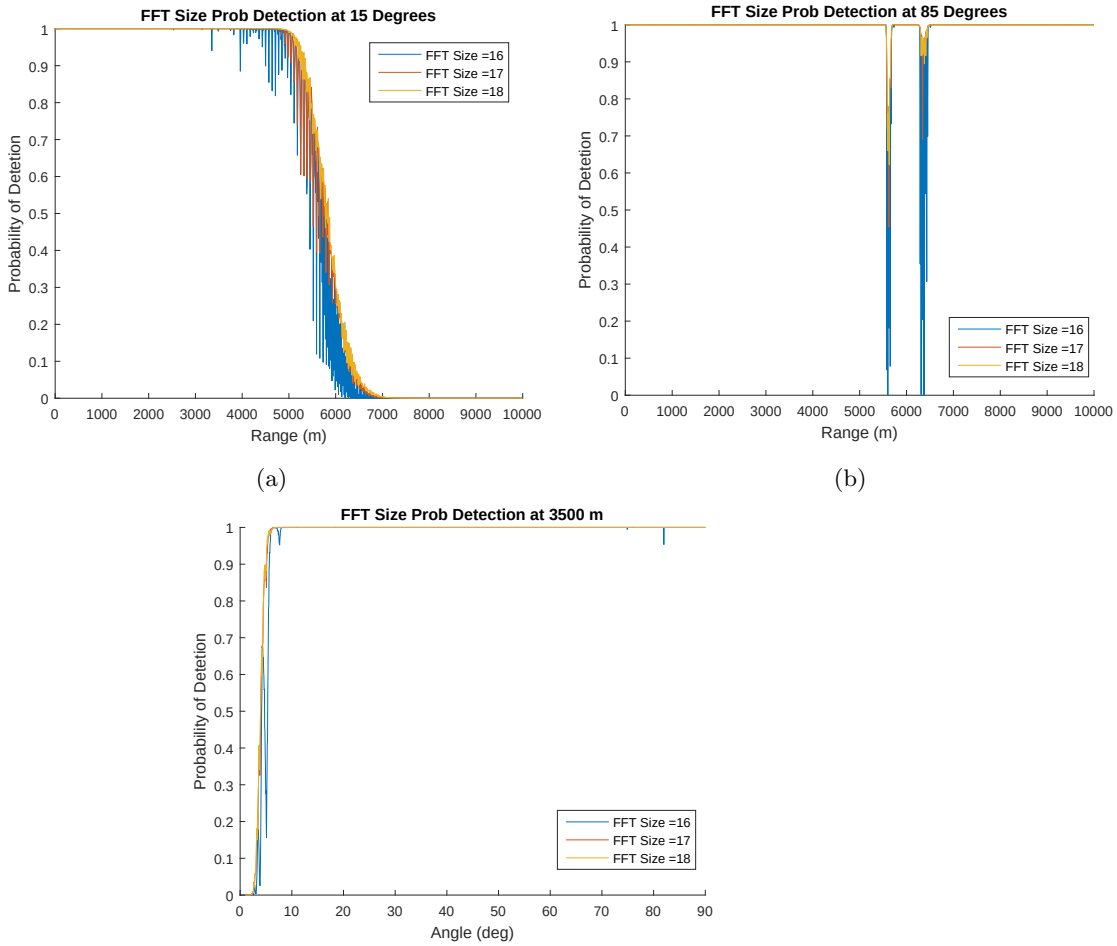

Fig. 4.8: Comparison of performance of FFT sizes. (a) Range varied from 5 to 10,000 m angle fixed at 15°. (b) Range varied from 5 to 10,000 m angle fixed at 85°. (c) Angle varied from 1° to 90° range fixed at 3500 m.

Table 4.5: False alarm rates for varying FFT sizes for the experiments shown in Fig. 4.8.

FFT Size	15° PFA	85° PFA	3500 m PFA
2^{16}	0.111e-8	0.107e-8	0.106e-8
2^{17}	0.445e-8	0.431e-8	0.425e-8
2^{18}	1.78e-8	1.72e-8	1.7e-8

CHAPTER 5

SCANNING PATTERNS

This chapter focuses on scanning parameters which could be used for an FMCW lidar in a planetary landing scenario. Traditionally the velocity vector would be obtained using an inertial measurement unit (IMU) but even well calibrated IMUs are subject to drift during the prolonged travel times incumbent upon space travel. An FMCW lidar can be used to obtain an estimate of the velocity vector of a spacecraft during the landing phase of the mission, but that requires a minimum of three measurements taken at different angles per velocity vector. After obtaining the radial velocity in three directions, a transformation can be performed on the data to redefine the vector in a better coordinate system, such as north east down. Three range measurements can also be used to obtain an estimate of the altitude of the craft.

5.1 NASA Morpheus Lidar

NASA's Morpheus test vehicle uses a lidar consisting of an optical head comprising three lidar transmitters which make a 45° cone angle [2–4]. Figure 5.1 shows the results of a simulation of the NASA three-beam lidar configuration. The instrument descends straight down from 500 m to 100 m starting at a velocity of 100 m/s and decelerates to 30 m/s, taking a measurement of each beam once per second. Figure 5.1(a) shows the descent path above the scene, while Figs. 5.1(b) and 5.1(c) show the point cloud colored by range and speed respectively.

One disadvantage of using a lidar which uses three beams is that if the measurement from one beam fails, a velocity vector and accurate estimate of altitude cannot be obtained. Adding extra beams provides redundancy and mitigates the risk of losing a velocity and altitude measurement. More beams also means that more of the terrain is "seen" by the lidar potentially allowing for some level of navigation or hazard avoidance. Another disadvantage

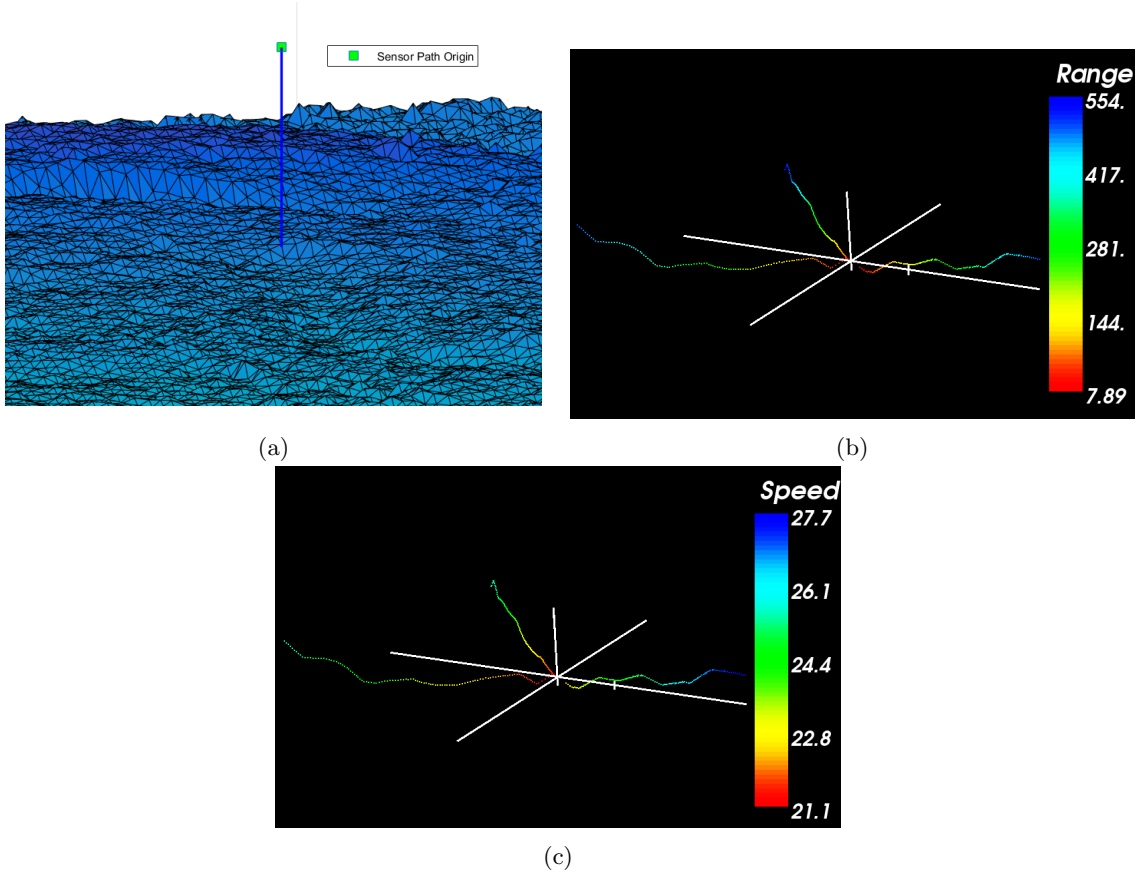

Fig. 5.1: Simulation results for the low altitude descent. The scanner uses a three-beam configuration with each beam at a 22.5° angle from nadir. The crosshairs point to an arbitrary point near the center of the cloud. The axes of the crosshairs have the same scaling and the tic is approximately 50 m from the crosshair origin. (a) Path to terrain. (b) Point cloud colored by range in meters. (c) Point cloud colored by velocity in meters per second. The point clouds are viewed from an oblique angle.

is that with the fixed telescopes, the scanning pattern cannot be changed. There may be some advantage in changing the beam pattern at different altitudes that cannot be achieved with a fixed beam pattern.

5.2 Non-mechanical Beam Steering

A solution to the disadvantages of the three beam fixed scanning pattern is to use a scanner to steer the beam. Having the ability to steer the beam allows for the scanning pattern to be changed at different phases of the descent and would allow for scanning patterns

which have more than three beams per measurement cycle for redundancy. A traditional scanner is a mechanical system generally consisting of several mirrors, at least one of them must rotate to change the direction of the beam, or mounting the telescope on a movable turret. Mechanical beam steering equipment is heavy and fragile, both huge disadvantages in a system that is to be launched into space. For this reason using a mechanical scanner is not a good solution to this problem.

A non-mechanical scanner is being developed for a landing scenario [17]. This scanner uses non-mechanical beam steering (NMBS) elements to point the beam plus or minus some angle along one axis. By stacking several of these NMBS elements on top of each other, some of them rotated 90° allows the beam to be directed along a grid of possible angles. Figure 5.2 shows a grid achieved by stacking four of these NMBS elements, two directing the beam ±15° on the vertical and horizontal axes respectively and two directing the beam ±7.5° on the vertical and horizontal axes respectively.

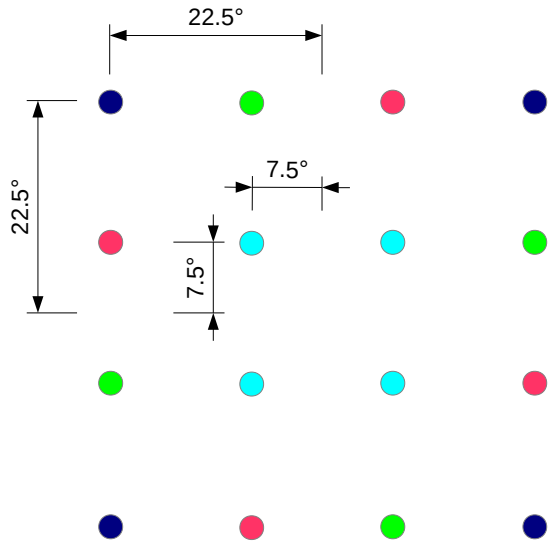

Fig. 5.2: Scan angles available with the NMBS.

The NMBS allows for much greater flexibility in scanning patterns and allows for the number of beams and the beam angles to be changed at any time. It has been proposed that fixed telescopes on NASA's FMCW Doppler lidar be replaced with the NMBS described above and use this modification to increase the beams per scan from three to four using either the $\pm 22.5^\circ$ scan angles shown in dark blue in Fig. 5.2 at altitudes above 500 m or the $\pm 7.5^\circ$ in scan angles shown in light blue in Fig. 5.2 at altitudes below 500 m.

5.2.1 Square Scanning Patterns

Several experiments were performed to produce point clouds illustrating the performance of the NMBS. In all examples the terrain used for the experiment shown in Fig. 5.1 was used. Several trajectories were simulated including vertical and 45° descents. Table 5.1 gives the parameters used in these simulations.

Table 5.1: Simulation parameters common to all of the simulations in Chapter 5.

Common Simulation Parameters		
Transmitter/Receiver	Aperture	50 mm
	Wavelength	1550 nm
	Transmitted Power	1 W
	Local Oscillator Power	1 mW
	Chirp Bandwidth (B)	1 GHz
	Chirp Start Frequency (F_1)	5.5 GHz
	Chirp Length (T)	500 μs
Detector	APD Gain	1 (pin diode)
	Electrical Bandwidth	400 MHz
	Responsivity	1.1 A/W
	Optical Passband	25 nm
	NEPD	5 pW/$\sqrt{\text{Hz}}$
Transimpedance Amplifier	Transimpedance Gain	7 kΩ
	Electrical Bandwidth	400 MHz
	Input Referred RMS Noise	25 nA
Range Processing	Sample Rate	600 MHz
	FFT Size	131,072
	Window Type	Hamming

In the first simulation, the lidar is pointed down and descends vertically from 2000 m to 500 m, with an initial velocity of 100 m/s and a constant deceleration to a final velocity of 32 m/s shown in Fig. 5.3. The measurement rate is set at 20 Hz, that is 20 measurements are taken per second. The beam scanning pattern are shown by the four dark blue outer corner points in Fig. 5.2. Each set of four measurements outlines the corners of a square on the ground. As the lidar descends, that square gets smaller. Figure 5.3(a) shows the flight path over the terrain. Figures 5.3(b) and 5.3(c) show the resulting point cloud colored by range and speed respectively. The coloring of these two point clouds looks similar because the speed is decreasing as the lidar moves closer to the ground. Figure 5.3(d) shows a close up of a segment of Fig. 5.3(b) where dropouts occur. The dropped detections occur when the lidar is at a relatively high altitude and may be attributed to a valley in detection probability as shown in Fig. 4.4(a), or a sloped surface in the simulated terrain.

The second simulation is similar to the first, but the lidar descends from 500 m to 10 m. This path is shown in Fig. 5.4(a). The scanner in this experiment uses the angles shown by the light blue inner square in Fig. 5.2. Using these inner angles allows for more data to be obtained about the terrain directly below the craft in order to potentially detect hazards in the landing site. Because this point cloud is more dense than those shown in Fig. 5.3, the effects of range quantization caused by binning of the FFT values are more evident as shown by Fig. 5.4(d).

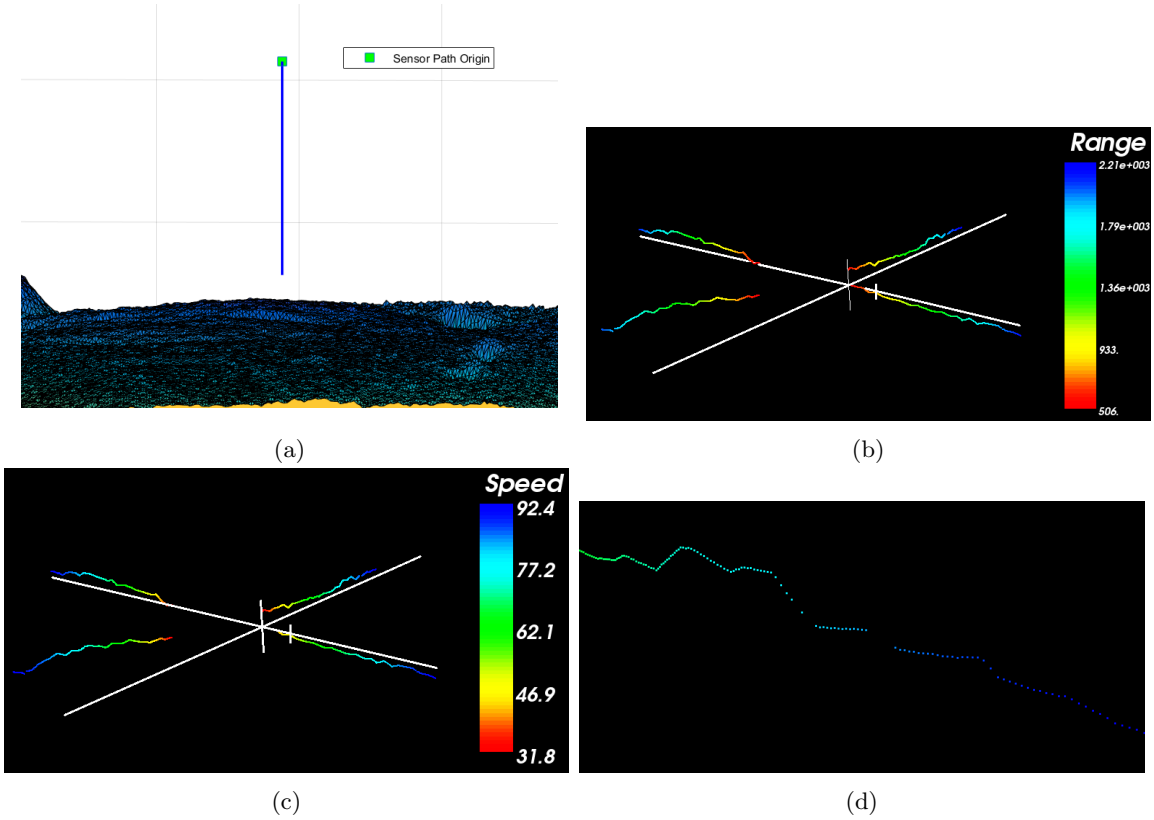

Fig. 5.3: Simulation results for the high altitude (2000 m) descent. The scanner uses a four-beam configuration with each beam at a 22.5° angle from nadir. The crosshairs point to an arbitrary point near the center of the cloud. The axes of the crosshairs have the same scaling and the tic is approximately 100 m from the crosshair origin. (a) Path to terrain. (b) Point cloud colored by range in meters. (c) Point cloud colored by radial velocity in meters per second. (d) Close-up of the range point cloud illustrating dropouts. The point clouds are viewed from an oblique angle.

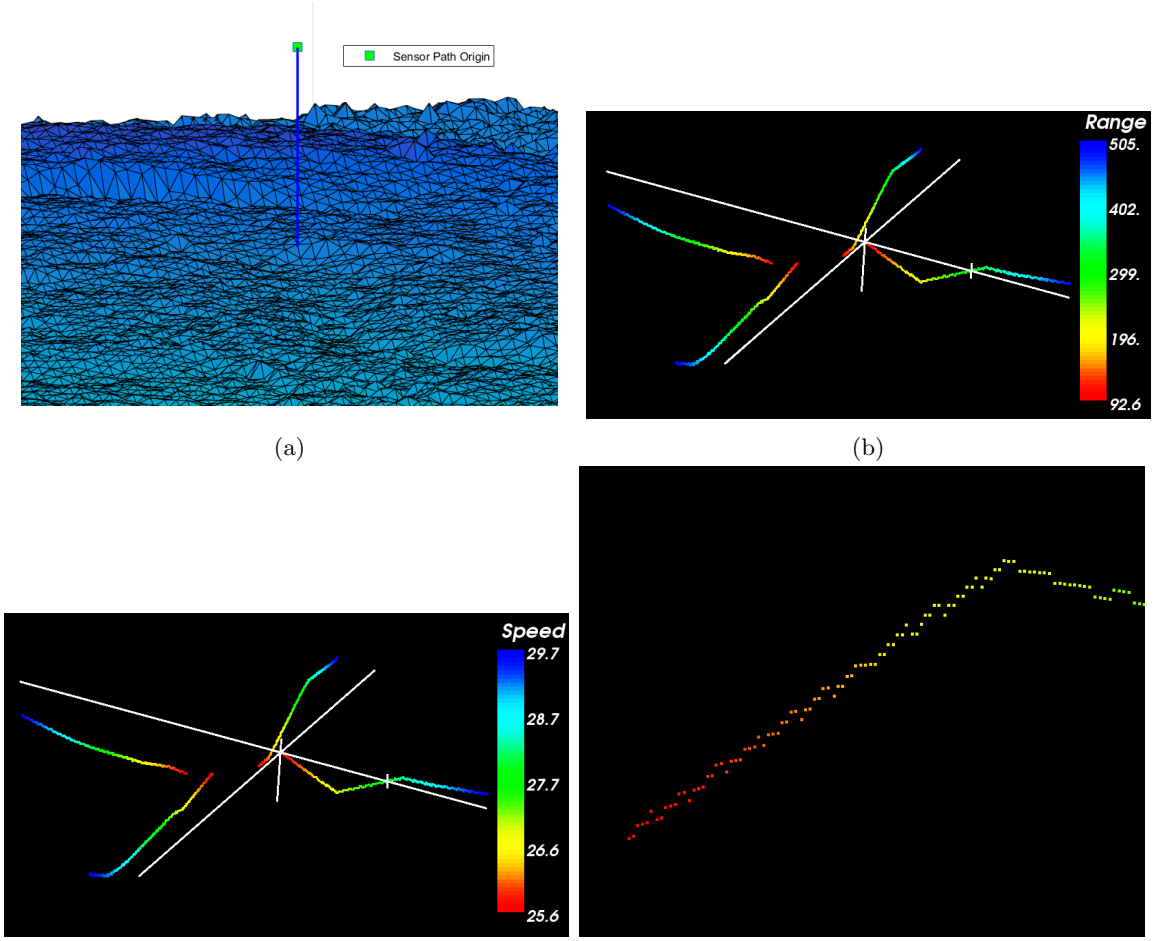

(a) (b)

(c) (d)

Fig. 5.4: Simulation results for the low altitude descent. The scanner uses a four-beam configuration with each beam at a 7.5° angle from nadir. The crosshairs point to an arbitrary point near the center of the cloud. The axes of the crosshairs have the same scaling and the tic is approximately 50 m from the crosshair origin. (a) Path to terrain. (b) Point cloud colored by range in meters. (c) Point cloud colored by radial velocity in meters per second. (d) Close-up of the range point cloud illustrating range quantization. The point clouds are viewed from an oblique angle.

Figure 5.5 shows an experiment where the lidar begins at 500 m and travels 400 m along a 45° path as seen in Fig. 5.5(a). The lidar in this simulation points directly down at the ground and measures the corners of a square defined by the inner angles shown in light blue in Fig. 5.2 while traveling in the direction of one of the square's diagonals. Because one beam points forward relative to the motion of the lidar, one beam points backward, and two beams point straight down relative to the forward direction of travel, the radial velocity seen by the three sets of beams is different. This can be seen in Fig. 5.5(c).

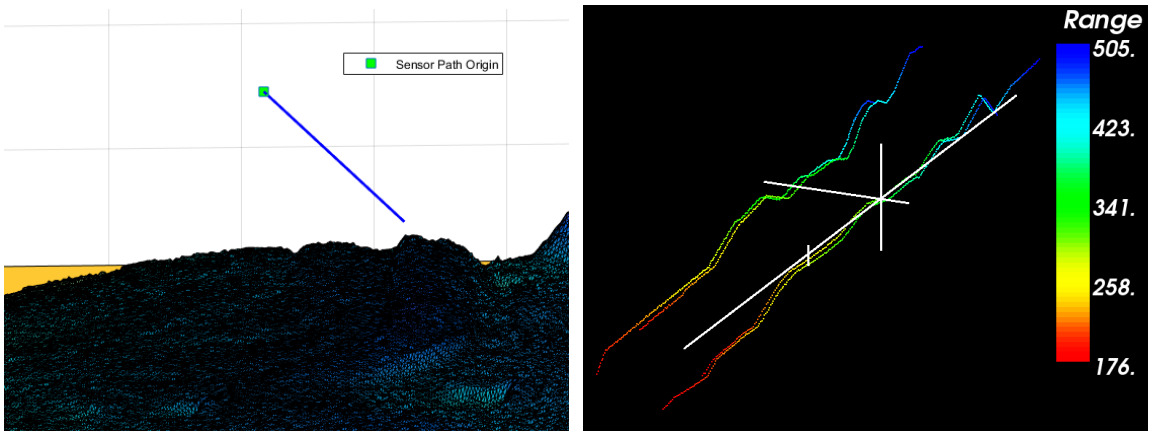

(a) (b)

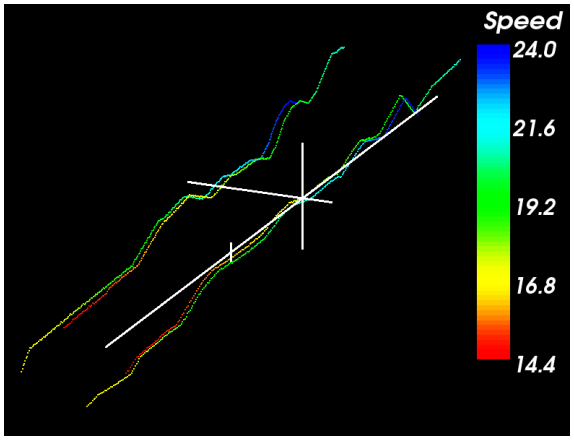

(c)

Fig. 5.5: Simulation results for the 45° descent starting at 500 m. The scanner uses a four-beam configuration with each beam at a 7.5° angle. The crosshairs point to an arbitrary point near the center of the cloud. The axes of the crosshairs have the same scaling and the tic is approximately 50 m from the crosshair origin. (a) 45° descent path. (b) Point cloud colored by range in meters. (c) Point cloud colored by radial velocity in meters per second. The point clouds are viewed from an oblique angle.

5.2.2 Expanded Scanning Pattern

The scanning patterns shown in the experiments of Section 5.2.1 use only 4 of the 16 angles made available by the NMBS. While these patterns are an improvement over the three beam fixed scanner currently used by NASA, they do not fully leverage the functionality of the NMBS.

A novel way to leverage the flexibility afforded by the NMBS is to cycle through all of the available pointing angles in a square pattern. The coloring of Fig. 5.2 shows this concept. First the dark blue points are sampled, then green, then red, and finally light blue. By cycling through these squares rather than just going point by point horizontally or vertically the angles at which sets of four measurements are sampled are more diverse, improving the accuracy of the estimation of the altitude and the velocity vector. By taking measurements at more angles more information about the terrain is gathered.

This scanning pattern was simulated with a flight path starting at 2000 m and descending straight down to 10 m with an initial velocity of 100 m/s and decelerating to a final velocity of 50 m/s. This simulation, as with the others in this chapter, produces each pattern at a rate of 20 Hz. The results of this simulation are shown in Fig. 5.6. As the lidar descends there is overlap between the patterns at 7.5° and 22.5°. This is recognizable in both point clouds shown in Fig. 5.6 by change in color mid way through each of the measurement lines from the four 22.5° where they meet the lines from the 7.5° corners.

The sampling pattern of the landing site is shown in Fig. 5.7. The landing site here is sampled much more densely than in the simulations using the square scanning patterns in Section 5.2.1. This simulation did not include atmospheric turbulence that a lander would experience when landing on a planetary body, such as Mars. Atmospheric turbulence would perturb the lidar's pointing angles and even more information about the terrain could be gathered. While the sampling of the landing site is not dense enough to map the terrain, it may be dense enough to detect significant hazards such as large boulders or cliffs.

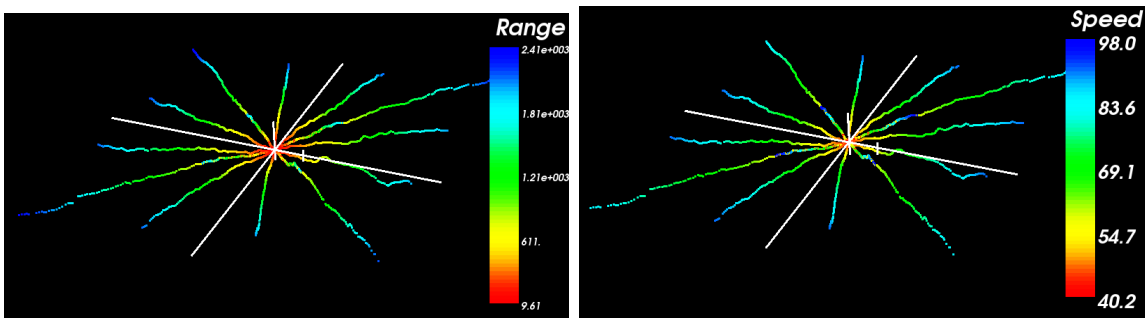

(a) (b)

Fig. 5.6: Simulation results for a 2000 m descent. The scanner uses 4 alternating patterns of 4 points each for 16 points. The crosshairs point to an arbitrary point near the center of the cloud. The axes of the crosshairs have the same scaling and the tic is approximately 100 m from the crosshair origin. (a) Point cloud colored by range in meters. (b) Point cloud colored by radial velocity in meters per second. These point clouds are viewed from an oblique angle.

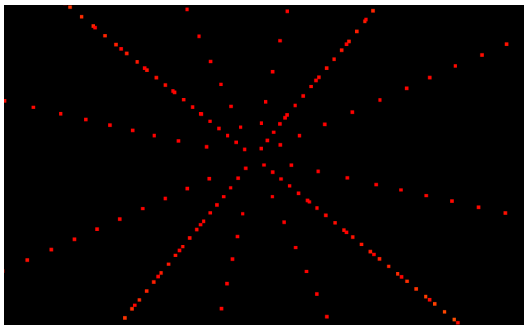

Fig. 5.7: Sampling pattern of the terrain as the lidar platform descends the last few meters viewed at an oblique angle.

CHAPTER 6
CONCLUSION

The purpose of this research project was to develop and add a simulation of an FMCW Doppler lidar transceiver to the LadarSIM software package and to use that simulation to investigate the effects transmission power, aperture diameter, and FFT size have on the performance of a Doppler lidar as well as simulate different scanning configurations and demonstrate their utility in a planetary landing scenario. This thesis has discussed the theory behind FMCW detection and demonstrated how an FMCW simulation was incorporated into LadarSIM. This chapter will provide a brief overview of the work done, discuss the results of the experiments, and suggest future work in the area.

6.1 Overview

Chapter 3 presents the work which was done to create the FMCW lidar transceiver simulation. In this chapter, the simulation process is outlined and the parameter GUIs are shown. Chapter 4 presents a trade-off study of 3 lidar parameters in terms of probabilities of detection and false alarm. Chapter 5 shows point clouds generated by running experiments on lidars with different scanning patterns in a planetary landing scenario.

6.2 Discussion of Results

The simulation created for this thesis is a useful tool to support many FMCW lidar projects. For someone designing a lidar for a particular planetary landing mission, LadarSIM can be used to determine what parameters the lidar must have. LadarSIM would also be a useful tool in the development of detection algorithms for FMCW lidar. An engineer could obtain detection spectra from LadarSIM and use those to test a given algorithm. The simulation would also be useful in determining the limits of an existing lidar system.

In Chapter 4, it was shown that transmission power and aperture diameter have a very

similar effect on the performance of a lidar system. The consequence of this is that if one of those parameters is constrained the other can be varied to compensate as necessary. The effect of FFT size on the performance of the system was also shown. This was interesting because it was expected that the FFT size would only affect the resolution of the system but because of scalloping loss, it does have an effect on the probability of dropout.

In Chapter 5, several scanning patterns were simulated. First, the three beam fixed telescope FMCW lidar which NASA currently uses was simulated. Then a non-mechanical beam steerer (NMBS) was presented and several scanning patterns using the NMBS were simulated and presented. As demonstrated by the point clouds in Section 5.2, the NMBS provides flexibility which, if properly leveraged, can allow an FMCW Doppler lidar to obtain more information about the terrain of the landing site than the three beam configuration as well as provide redundancy to mitigate the effects of beam dropout.

6.3 Future Work

LadarSIM is a useful tool and has been in development at Utah State University's Center for Advanced Imaging Ladar over the past decade and a half [5, 6]. LadarSIM already included a simulation of time of flight (TOF) lidar before the work of this thesis. The FMCW Doppler lidar simulation could be improved by adding the following:

- A more thorough model of the probability of false alarm.
- A simulation of laser speckle.
- The simulation of alternative spectrum estimation methods, such as the Chirped Z method [18]
- The simulation of alternative detection algorithms.

These additions would improve upon the accuracy and versatility of LadarSIM's Doppler lidar simulation.

REFERENCES

[1] P. Adany, *Simplified homodyne detection for FM chirped lidar*. ProQuest, 2007.

[2] F. Amzajerdian, L. Petway, G. Hines, B. Barnes, D. Pierrottet, and G. Lockard, "Doppler lidar sensor for precision landing on the moon and mars," in *2012 IEEE Aerospace Conference*, March 2012, pp. 1–7.

[3] F. Amzajerdian, D. Pierrottet, L. Petwat, G. Hines, B. Barnes, and G. Lockard, "Fiber doppler lidar for precision navigation of space vehicles," in *Lasers, Sources, and Related Photonic Devices*. Optical Society of America, 2012, p. FTh3.1A.2. [Online]. Available: http://www.osapublishing.org/abstract.cfm?URI=FILAS-2012-FTh3.1A.2

[4] F. Amzajerdian, L. Petway, G. Hines, B. Barnes, D. Pierrottet, and G. Lockard, "Doppler lidar sensor for precision landing on the moon and mars," in *2012 IEEE Aerospace Conference*, March 2012, pp. 1–7.

[5] S. Budge, B. Leishman, and R. Pack, "Simulation and modeling of return waveforms from a ladar beam footprint in usu ladarsim," pp. 62 140N–62 140N–10, 2006. [Online]. Available: http://dx.doi.org/10.1117/12.666404

[6] K. D. Neilsen, S. E. Budge, R. T. Pack, R. R. Fullmer, and T. D. Cook, "Design and validation of the eyesafe ladar testbed (elt) using the ladarsim system simulator," pp. 73 230B–73 230B–7, 2009. [Online]. Available: http://dx.doi.org/10.1117/12.818856

[7] G. Brooker, "Introduction to sensors for ranging and imaging," 2009.

[8] F. Amzajerdian, D. Pierrottet, G. Hines, L. Petway, and B. Barnes, "Doppler lidar sensor for precision navigation in gps-deprived environment," in *SPIE Defense, Security, and Sensing*. International Society for Optics and Photonics, 2013, pp. 87 310G–87 310G.

[9] P. Adany, C. Allen, and R. Hui, "Chirped lidar using simplified homodyne detection," *Journal of Lightwave Technology*, vol. 27, no. 16, pp. 3351–3357, Aug 2009.

[10] C. Allen, Y. Cobanoglu, S. K. Chong, and S. Gogineni, "Performance of a 1319 nm laser radar using rf pulse compression," in *IGARSS 2001. Scanning the Present and Resolving the Future. Proceedings. IEEE 2001 International Geoscience and Remote Sensing Symposium (Cat. No.01CH37217)*, vol. 3, 2001, pp. 997–999 vol.3.

[11] F. Amzajerdian, D. Pierrottet, G. D. Hines, L. Petway, and B. W. Barnes, "Coherent doppler lidar for measuring velocity and altitude of space and arial vehicles," 2016.

[12] D. Pierrottet, F. Amzajerdian, L. Petway, B. Barnes, and G. Lockard, "Flight test performance of a high precision navigation doppler lidar," in *SPIE Defense, Security, and Sensing*. International Society for Optics and Photonics, 2009, pp. 732 311–732 311.

[13] D. Pierrottet, F. Amzajerdian, L. Petway, B. Barnes, G. Lockard, and G. Hines, "Navigation doppler lidar sensor for precision altitude and vector velocity measurements: flight test results," in *SPIE Defense, Security, and Sensing*. International Society for Optics and Photonics, 2011, pp. 80 440S–80 440S.

[14] G. Di Domenico, S. Schilt, and P. Thomann, "Simple approach to the relation between laser frequency noise and laser line shape," *Applied optics*, vol. 49, no. 25, pp. 4801–4807, 2010.

[15] M. A. Richards, "The discrete-time fourier transform and discrete fourier transform of windowed stationary white noise," *Georgia Institute of Technology, Tech. Rep*, 2007.

[16] Y. Wang, Z. Xiao, and J. Xu, "A novel threshold detection method for fmcw radar," in *IET International Radar Conference 2015*, Oct 2015, pp. 1–5.

[17] S. E. Budge and D. B. Chester, "Simulation of a doppler lidar system for autonomous navigation and hazard avoidance during planetary landing," in *SPIE Defense+ Security*. International Society for Optics and Photonics, 2016, pp. 983 208–983 208.

[18] P.-C. Gong, J. Li, W. Guo, and Z. Shao, "A high resolution algorithm based on chirp z-transform for fmcw radar," in *Communication Problem-Solving (ICCP), 2015 IEEE International Conference on.* IEEE, 2015, pp. 482–484.